

1
2
3
4
5
6
7
8
9
10
11
12
13
14
15
16
17
18
19
20
21
22
23
24
25

UNIVERSITY OF CALIFORNIA
SANTA CRUZ

**AN INCLUSIVE SEARCH FOR THE DECAY OF A BOOSTED
HIGGS BOSON IN THE $H \rightarrow b\bar{b}$ CHANNEL WITH THE ATLAS
DETECTOR**

A dissertation submitted in partial satisfaction of the
requirements for the degree of
DOCTOR OF PHILOSOPHY

in

PARTICLE PHYSICS

by

Jacob Martin Pasner

October 2019

The Dissertation of Jacob Martin Pasner
is approved:

Professor Jason Nielsen, Chair

Professor Abraham Seiden

Professor Michael Hance

Dean Lori Kletzer
Vice Provost and Dean of Graduate Studies

Copyright © by

Jacob Martin Pasner

2019

31 **Table of Contents**

32	List of Figures	vii
33	List of Tables	x
34	Abstract	xi
35	Dedication	xii
36	Acknowledgments	xiii
37	1 Introduction	1
38	I Theoretical Motivations and the Standard Model	2
39	2 The Standard Model and Beyond	3
40	2.1 The Standard Model	4
41	2.1.1 Bosons	5
42	2.1.2 Fermions	8
43	2.2 Quantum Electrodynamics	8
44	2.3 Quantum Chromodynamics	12
45	2.4 The Higgs Mechanism	14

46	2.4.1	Electroweak Symmetry Breaking	14
47	2.4.2	Fermion Mass Terms	18
48	2.4.3	The Higgs Boson	19
49	3	Boosted Higgs at the LHC	21
50	3.1	Higgs Production Mechanisms	22
51	3.2	Parton Distribution Function	25
52	3.3	Branching Ratios	25
53	3.4	Discovery	28
54	3.5	Boosted Higgs	28
55	II	Experimental Apparatus and Associated Facilities	29
56	4	The Large Hadron Collider	30
57	4.1	Particle Incjection Chain	31
58	4.2	LHC layout and design	33
59	4.3	Performance	36
60	4.4	Pile-up at the LHC	38
61	5	The ATLAS Detector	40
62	5.1	ATLAS Coordinate System	43
63	5.2	Tracking with the Inner Detector	47
64	5.2.1	Pixel Detector	49
65	5.2.2	Semiconductor Tracker	49
66	5.2.3	Transition Radiation Tracker	50
67	5.3	Calorimetry	51
68	5.3.1	Electromagnetic Calorimeter	52

69	5.3.2 Hadronic Calorimeter	54
70	5.4 Muon Spectrometer	56
71	III The HbbISR Analysis	59
72	6 Data and Simulation Preparation	60
73	6.1 Data Used	60
74	6.2 Monte Carlo Samples	60
75	7 Physics Object Selection	61
76	7.1 Calorimeter Jets	62
77	7.2 Track Jets	62
78	7.3 Fat Jets	62
79	7.4 B-tagged Jets	62
80	7.5 Muons	62
81	7.6 Overlap Removal	62
82	8 Event Selection	63
83	8.1 Selected Triggers	63
84	8.2 Pre-selection Studies	63
85	8.3 Signal Selection	63
86	8.4 Optimisation	63
87	9 Background Estimation	64
88	9.1 Multi-jet QCD estimation	64
89	9.2 $t\bar{t}$ control region	64
90	9.3 Single top estimation	64
91	9.4 Hadronic vector boson channel	64

92	10 Systematic Uncertainties	65
93	10.1 Theoretical Uncertainties	65
94	10.2 Experimental Uncertainties	65
95	11 Statistical Fit	66
96	11.1 Profile Likelihood Function	66
97	11.2 Fit Configuration	66
98	11.3 Statistical Tests	66
99	12 Results	67
100	12.1 Expectations	67
101	12.2 Statistical Analysis Results	67
102	12.3 Measurements and Limits	67
103	IV Conclusion	68
104	13 Conclusion	69
105	Bibliography	69
106	A Hadronic Vqq Sherpa Studies	72

107 List of Figures

108	2.1	Summary of several Standard Model total and fiducial production cross	
109		section measurements, corrected for leptonic branching fractions, com-	
110		pared to the corresponding theoretical expectations. All theoretical ex-	
111		pectations were calculated at NLO or higher. The dark-color error bar	
112		represents the statistical uncertainty. The lighter-color error bar repre-	
113		sents the full uncertainty, including systematics and luminosity uncer-	
114		tainties. The data/theory ratio, luminosity used and reference for each	
115		measurement are also shown. Uncertainties for the theoretical predictions	
116		are quoted from the original ATLAS papers. They were not always eval-	
117		uated using the same prescriptions for PDFs and scales. The Wgamma	
118		and Zgamma theoretical cross-sections have non-perturbative corrections	
119		applied to the NNLO fixed order calculations (PRD 87, 112003 (2013)).	
120		Not all measurements are statistically significant yet.	6
121	2.2	Table of all observed fundamental particles of the current Standard Model.	7
122	2.3	A lower dimensionality representation of the shape of the Higgs Potential.	
123		The central peak represents a $v = 0$ rotationally symmetric unstable	
124		state, while the trough represents the infinite choices of minima that can	
125		be selected upon the spontaneous breaking of symmetry.	15
126	3.1	Cross section for the production of the SM Higgs boson as a function of	
127		the center of mass energy (\sqrt{s}) at the LHC. [1]	22
128	3.2	Feynman diagrams representing the dominant Higgs production modes	
129		at the LHC.	23

130	3.3	[2] MMHT2014 NNLO PDFs at $Q^2 = 10\text{GeV}^2$ and $Q^2 = 10^4\text{GeV}^2$ with	
131		associated 68% confidence-level uncertainty bands. The colored regions	
132		indicate the probability of finding the labeled parton with a momentum	
133		fraction given along the x axis. As expected the u_V and d_V contain the	
134		largest fraction of the momentum, however we can also see that many	
135		gluons will exist with smaller fractions of the total momentum. Note	
136		that as Q^2 increases you are more likely to find something besides a u/d	26
137	3.4	Feynman diagrams representing the leading Higgs decay channels. . . .	27
138	4.1	CERN accelerator complex	32
139	4.2	Labeled diagram of all the experiments at the LHC indicating the counter	
140		circulating beams and points of interest along the circumference of the	
141		accelerator.	34
142	4.3	Depiction of a LHC dipole magnet 2-in-1 design labeling the major com-	
143		ponents	35
144	4.4	Luminosity is monitored as both a running total known as the Integrated	
145		Luminosity as depicted in (a) and as an instantaneous quantity as shown	
146		in (b)	38
147	4.5	Pileup for data taking periods 2015 - 2018	39
148	5.1	[5] Here we see a cut-away side view of the ATLAS detector with the	
149		major components labeled. Note that within each of these labeled com-	
150		ponents there may exist multiple different detector technologies. For scale	
151		two people in red are shown standing between the disk muon chambers	
152		on the left side of the figure.	41
153	5.2	This slice of the ATLAS detector depicts how different particles interact	
154		with each component of the detector it crosses. A dashed line indicates	
155		no interaction while a solid line indicates interaction. Electrons (yel-	
156		low/green) and charged hadrons (red) interact with the tracker and curve	
157		in the solenoid's magnetic field. Electrons and photons (yellow/green) are	
158		absorbed by the Electromagnetic calorimeter. All hadrons (red/yellow)	
159		are absorbed by the Hadronic calorimeter. The muons (orange) curve in	
160		both the solenoid and torroid magnetic fields before exiting the detector.	
161		Finally, the neutrinos (white) pass through the entire detector without	
162		interacting.	44

163	5.3	[6] A cartoon view of the the LHC from above showing the SPS, LHC	
164		and the four main experiments of the LHC: ATLAS, CMS, LHCb, and	
165		ALICE. The standard cartesian coordinate system is shown with its origin	
166		at the ATLAS interaction point, the positive x -axis towards the center	
167		of the LHC, the positive y -axis pointing upwards, and the positive z -axis	
168		pointing along the beamline towards the "A-side"	45
169	5.4	Modified from [6] this cartoon represents a selection of pseudorapidity	
170		(η) values overlaid with some cartesian coordinates (dashed black lines).	
171		The redlines are drawn for $\eta = \pm 0.5, 1.0, 3.0$	46
172	5.5	[7] Diagram of inner detector	47
173	5.6	[10] Schematic of the Inner Detector including eta lines. Each component	
174		shown is cylindrically symmetric leading to a multi-layered detector. . .	48
175	5.7	[5] A cutaway diagram of ATLAS's sampling calorimeters	51
176	5.8	[5] Sketch of LAr EMC barrel module where the lead and liquid argon	
177		layers are visible in an accordion like geometry. Looking from the fore-	
178		ground to the back there are 3 different types of cells visible.	53
179	5.9	[5] Schematic of a tile calorimeter module including a depiction of the con-	
180		nection between the scintillator tile to the photomultiplier via a wavelength-	
181		shifting fibre.	55
182	5.10	[5] A cut-away diagram of the ATLAS muon system and its many sub-	
183		detectors.	57

184 **List of Tables**

185	3.1	The branching ratios and the relative uncertainty for a Standard Model	
186		Higgs boson with $m_H = 125$ GeV.	28

187

Abstract

188

An Inclusive Search for the decay of a Boosted Higgs boson in the $H \rightarrow b\bar{b}$

189

channel with the ATLAS detector

190

by

191

Jacob Martin Pasner

192

Abstract placeholder

193

Dedication

194

Dedication

195

Dedication

Acknowledgments

197 Chapter 1

198 Introduction

199 Every dissertation should have an introduction. You might not realize it, but the
200 introduction should introduce the concepts, backgrouand, and goals of the dissertation.

201

Part I

202

Theoretical Motivations and the

203

Standard Model

Chapter 2

The Standard Model and Beyond

The Standard Model (SM) of Particle Physics is humanities best "guess" at the force laws that describe the observed behavior of all particles in our universe. Its formulation is a collection of Quantum Field Theories (QFT) that describe the following interactions of elementary matter in Nature: the electromagnetic force, the weak nuclear force and the strong nuclear force. Gravity is noticeably absent as currently there is no viable quantum theory for observed gravitational effects. The Glashow-Salam-Weinberg (GSW) theory of Quantum Electrodynamics (QED) describes the electromagnetic and weak forces, while Quantum Chromodynamics (QCD) describes the strong force. These theories form the following symmetry group of the Standard Model.

$$\underbrace{\mathrm{SU}_C(3)}_{\mathrm{QCD}} \otimes \underbrace{\mathrm{SU}_L(2) \otimes \mathrm{U}_Y(1)}_{\mathrm{GSW}}. \quad (2.1)$$

215 The gauge principle states that the SM Lagrangian and its predictions must be invariant
216 under local transformations using an operator from any of these constituent groups.
217 Thus, any theory must only include transformations and terms that maintain the local
218 invariance of the complete Lagrangian. In particular, this requirement was violated
219 by any attempt to include an explicit mass term for the Gauge Bosons of QED and
220 for all fermions. Around 1960 a possible solution to this lack of mass was proposed
221 in the form of the spontaneous breaking of the ElectroWeak symmetry, now known as
222 the Higgs mechanism. In the following sections I will go into more detail about the
223 Lagrangian formalism of the Standard Model, QCD, QED and this recently verified
224 Higgs Mechanism.

225 **2.1 The Standard Model**

226 At the turn of the 20th century our understanding of the constituent matter of the uni-
227 verse was limited to what we could see with microscopes and imply from the observations
228 of light and electricity, giving us evidence for both the photon and the electron. In the
229 first half of the century we discovered the field of subatomic physics with Rutherford's
230 1911 gold foil scattering experiment, and Dirac successfully demonstrated the quantiza-
231 tion of the electromagnetic field, the first step towards a fully Gauge Invariant Quantum
232 Field Theory. In the second half we literally delved deeper, discovering that the nucleus
233 contained structure and extended our theories to include the the complex mechanics of
234 quarks and gluons. With the discovery of the Higgs in 2013 the Standard Model has

235 become an irrefutable framework as can be seen in the high level of agreement between
236 theory and experiment in fig. 2.1.

237 The QCD and QED theories predict two classes of particles: fermions and bosons shown
238 in fig. 2.2. These particles represent the quanta of the quantum fields of the Standard
239 Model and the mediators of the fundamental forces of Nature.

240 **2.1.1 Bosons**

241 These spin-1 particles are known as the vector gauge bosons and are the force carriers
242 of the SM. The most commonly known is the electromagnetic force's un-charged and
243 massless photon (γ) which interacts with all charged particles and is often referred to
244 as "light". The weak nuclear force is involved in nuclear interactions such as beta
245 decays and is carried by 3 bosons all of which have mass and couple to all fermions;
246 the W^\pm bosons, which mediate the charged weak nuclear interaction and allow for
247 flavor changing currents; and the Z boson which mediates the neutral weak nuclear
248 interaction. Finally we have 8 massless gluons which mediate the strong nuclear force
249 and only interact with fermions with a "color" charge such as the quarks contained
250 inside the nucleus. The only spin-0 boson, the Higgs Boson (h) is the key to generating
251 mass terms in the SM Lagrangian for the massive Gauge Bosons and for fermions.
252 This is done through the so called Higgs Mechanism and is discussed in more detail in
253 section 2.4.

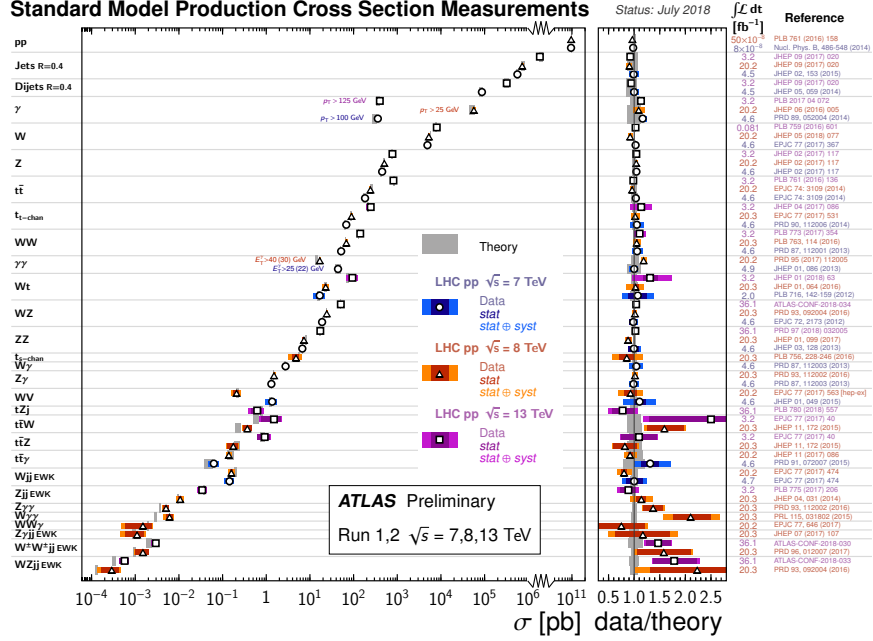


Figure 2.1: Summary of several Standard Model total and fiducial production cross section measurements, corrected for leptonic branching fractions, compared to the corresponding theoretical expectations. All theoretical expectations were calculated at NLO or higher. The dark-color error bar represents the statistical uncertainty. The lighter-color error bar represents the full uncertainty, including systematics and luminosity uncertainties. The data/theory ratio, luminosity used and reference for each measurement are also shown. Uncertainties for the theoretical predictions are quoted from the original ATLAS papers. They were not always evaluated using the same prescriptions for PDFs and scales. The $W\gamma$ and $Z\gamma$ theoretical cross-sections have non-perturbative corrections applied to the NNLO fixed order calculations (PRD 87, 112003 (2013)). Not all measurements are statistically significant yet.

Standard Model of Elementary Particles

three generations of matter (fermions)						interactions / force carriers (bosons)	
I		II		III			
mass	$\approx 2.2 \text{ MeV}/c^2$	$\approx 1.28 \text{ GeV}/c^2$	$\approx 173.1 \text{ GeV}/c^2$	0	$\approx 124.97 \text{ GeV}/c^2$		
charge	$\frac{2}{3}$	$\frac{2}{3}$	$\frac{2}{3}$	0	0		
spin	$\frac{1}{2}$	$\frac{1}{2}$	$\frac{1}{2}$	1	0		
QUARKS							
	up	charm	top	gluon	higgs		
	$\approx 4.7 \text{ MeV}/c^2$	$\approx 96 \text{ MeV}/c^2$	$\approx 4.18 \text{ GeV}/c^2$	0			
	$-\frac{1}{3}$	$-\frac{1}{3}$	$-\frac{1}{3}$	0			
	$\frac{1}{2}$	$\frac{1}{2}$	$\frac{1}{2}$	1			
	down	strange	bottom	photon			
LEPTONS	$\approx 0.511 \text{ MeV}/c^2$	$\approx 105.66 \text{ MeV}/c^2$	$\approx 1.7768 \text{ GeV}/c^2$	$\approx 91.19 \text{ GeV}/c^2$	SCALAR BOSONS		
	-1	-1	-1	0			
	$\frac{1}{2}$	$\frac{1}{2}$	$\frac{1}{2}$	1			
electron	muon	tau	Z boson				
$<2.2 \text{ eV}/c^2$	$<0.17 \text{ MeV}/c^2$	$<18.2 \text{ MeV}/c^2$	$\approx 80.39 \text{ GeV}/c^2$	GAUGE BOSONS VECTOR BOSONS			
0	0	0	± 1				
	$\frac{1}{2}$	$\frac{1}{2}$	1				
	electron neutrino	muon neutrino	tau neutrino	W boson			

Figure 2.2: Table of all observed fundamental particles of the current Standard Model.

254 2.1.2 Fermions

255 These spin-1/2 particles can be further broken up into two distinct families of particles,
256 the leptons and the quarks, both of which contain three "generations" each with an "up"
257 and "down" type particle. The leptons "up" type members are the electrically charged
258 electron (e), muon (μ) and tau (τ) while the "down" type are their electrically neutral
259 counterparts ν_e , ν_μ , ν_τ . The quarks "up" type members are the up (u), charm (c),
260 and top (t) each with a $+2/3$ elementary charge, while the "down" type members are
261 the down (d), strange (s), and bottom (b) all of which have a $-1/3$ elementary charge.
262 Each quark carries a "color" charge thus allowing them to participate in strong force
263 interactions. Due to the observed color confinement of the strong force these quarks are
264 only observed in colorless bound states known as "mesons" (1 quark and 1 anti-quark)
265 and "baryons" (an odd number of quarks and anti-quarks). All of the above fermions
266 have an anti-particle partner which has the opposite electrical charge but is otherwise
267 identical.

268 2.2 Quantum Electrodynamics

269 In the SM the Electromagnetic and Weak nuclear forces are unified into the Electroweak
270 interaction which is represented by the $SU(2)_L \times U(1)_Y$ gauge group. The L represents
271 the physical observable that the Weak interaction, and thus the $SU(2)$ transformation,
272 only acts on left handed particle states. The Y states that this is the $U(1)$ symmetry

273 for the weak hypercharge Y instead of the electromagnetic charge. The particle states
 274 for these interactions are solutions to the Dirac equation and are represented as Dirac
 275 spinor doublets (Ψ_L) for the left handed states, and as Dirac spinor singlets (Ψ_R) for
 276 the right handed states. Thus when a general transformation from the Electroweak
 277 gauge group is applied to the left handed spinor doublet you get eq. (2.2)

$$\Psi_L \rightarrow \Psi'_L = \exp \left(\underbrace{ig' \frac{Y_L}{2} \zeta(x)}_{U(1)_Y} + \underbrace{ig_W \boldsymbol{\alpha}(x) \cdot \mathbf{T}}_{SU(2)_L} \right) \Psi_L. \quad (2.2)$$

278 For the right handed spinor singlet the $SU(2)_L$ doesn't contribute and you get eq. (2.3)

$$\Psi_R \rightarrow \Psi'_R = \exp \left(\underbrace{ig' \frac{Y_R}{2} \zeta(x)}_{U(1)_Y} \right) \Psi_R. \quad (2.3)$$

279 We can see that these local gauge transformations have introduced space-time depen-
 280 dant terms $\boldsymbol{\alpha}(x)$ and $\zeta(x)$ into our electroweak Lagrangian. Due to the derivatives
 281 contained within the kinetic term of this lagrangian, this new configuration would in-
 282 troduce additional terms, thus violating our required local gauge invariance. Luckily,
 283 we can remove these additional terms by replacing the standard derivative (∂_μ) with th
 284 covariant derivative (D_μ) as seen in eq. (2.4) for the left handed states and eq. (2.5) for
 285 the right handed states.

$$D_\mu = \partial_\mu - \underbrace{\frac{1}{2}ig' B_\mu Y_L}_{U(1)_Y} - \underbrace{\frac{1}{2}ig_W \mathbf{W}_\mu \cdot \boldsymbol{\tau}}_{SU(2)_L} \quad (2.4)$$

$$D_\mu = \partial_\mu - \underbrace{\frac{1}{2}ig' B_\mu Y_R}_{U(1)_Y} \quad (2.5)$$

286 Here we see two new gauge fields; B_μ the weak hypercharge field and \mathbf{W}_μ the charged
 287 weak field as well as the associated coupling constants g', g_W, Y_L, Y_R and the $SU(2)$
 288 generators $\boldsymbol{\tau}$. Next we write down the transformation properties of these new fields

$$\mathbf{W}_\mu(x) \rightarrow \mathbf{W}'_\mu(x) = \mathbf{W}_\mu + \partial_\mu \boldsymbol{\alpha}(x) + g_W \mathbf{W}_\mu(x) \times \boldsymbol{\alpha}(x) \quad (2.6)$$

$$B_\mu \rightarrow B'_\mu = B_\mu + \frac{1}{g'} \partial_\mu \zeta(x) \quad (2.7)$$

289 The form of these fields is chosen such that the final Lagrangian is invariant under
 290 $SU(2)_L \times U(1)_Y$ transformations, and thus we have restored gauge invariance for the
 291 kinetic term of our electroweak Lagrangian! Inserting these new definitions into the
 292 Lagrangian for the spinor field Ψ which satisfies the free-particle Dirac equation we get

$$\mathcal{L} = i\bar{\Psi}_L \gamma^\mu \left(\partial_\mu - \frac{1}{2}ig' B_\mu Y_L - \frac{1}{2}ig_W \mathbf{W}_\mu \cdot \boldsymbol{\tau} \right) \Psi_L + i\bar{\Phi}_R \gamma^\mu \left(\partial_\mu - \frac{1}{2}ig' B_\mu Y_R \right) \Phi_R \quad (2.8)$$

293 Next we must construct the gauge field self interaction and mass terms

$$\mathcal{L} = -\frac{1}{4}\mathbf{F}_{\mu\nu}\mathbf{F}^{\mu\nu} - \frac{1}{4}B_{\mu\nu}B^{\mu\nu} + \frac{1}{2}M_W^2\mathbf{W}_\mu\mathbf{W}^\mu + \frac{1}{2}M_B^2B_\mu B^\mu \quad (2.9)$$

294 where the field tensors $\mathbf{F}^{\mu\nu}$ and $B^{\mu\nu}$ are defined to be

$$\mathbf{F}^{\mu\nu} = \partial^\mu\mathbf{W}^\nu - \partial^\nu\mathbf{W}^\mu + g\mathbf{W}^\mu \times \mathbf{W}^\nu \quad (2.10)$$

$$B^{\mu\nu} = \partial^\mu B^\nu - \partial^\nu B^\mu \quad (2.11)$$

295 The field tensor terms in eq. (2.9) are invariant under our gauge transformations, but
 296 simply plugging in eq. (2.4) or eq. (2.5) into the mass terms shows that these terms
 297 violate gauge invariance thus implying $M_W = 0$ and $M_B = 0$ in direct contradiction of
 298 the observed masses of the weak gauge bosons. This issue arises again for fermion mass
 299 terms as illustrated below for the electron field (e) expanded in its chiral basis.

$$m_e\bar{e}e = m_e \begin{pmatrix} e_R^\dagger & e_L^\dagger \end{pmatrix} \begin{pmatrix} e_L \\ e_R \end{pmatrix} = m_e(e_R^\dagger e_L + e_L^\dagger e_R) \quad (2.12)$$

300 Remembering that the left and right handed spinors of the electroweak interaction trans-
 301 form differently we see that this mixture of right and left fields violates gauge invariance.
 302 This again forces us to conclude that $m_e = 0$ in contradiction to the observation that
 303 the electron does indeed have mass. As mentioned in section 2.1.1 the resolution to
 304 these mass mysteries lies in the Higgs mechanism discussed in section 2.4

305 2.3 Quantum Chromodynamics

306 Quantum Chromodynamics is the continuation of the mathematical framework estab-
 307 lished by Quantum Electrodynamics (section 2.2, this time for the strong force described
 308 by the $SU(3)_C$ gauge group where the C represents the "color" charge of QCD. This
 309 color charge doesn't imply actual visible color, but is useful as an analogy to the visible
 310 spectrum where a combination of red, green, and blue generates white. For QCD the
 311 combination of red, green, and blue color charges results in a colorless object. As men-
 312 tioned in section 2.1.2 the quarks will contain a color (anti-color) charge represented by
 313 a color triplet field which transforms under the general $SU(3)$ transformation as shown
 314 here

$$q = \begin{pmatrix} q_r \\ q_g \\ q_b \end{pmatrix} \rightarrow q' = \exp \left(ig_s \sum_{k=1}^8 \eta_k(x) \frac{\lambda_k}{2} \right) q \quad (2.13)$$

315 Here the λ_k are the generators for $SU(3)$, $\eta(x)_k$ is the space-time dependency for each
 316 generator, and g_s is the strong coupling constant. As with QED, the introduction of
 317 these space-time dependant terms introduces new terms into the kinematic portion of
 318 the lagrangian thus spoiling our gauge invariance. Again, we introduce a covariant

319 derivative to restore invariance

$$D_\mu = \partial_\mu - ig_s G_\mu^k \frac{\lambda_k}{2} \quad (2.14)$$

320 Here the G_μ^k are the new fields introduced for the 8 gluons. These new fields transform
321 under $SU(3)$ as shown in eq. (2.15)

$$G_\mu^k \rightarrow G_\mu'^k = G_\mu^k + \partial_\mu \eta_k(x) + g_s f_{klm} \eta_l(x) G_\mu^m \quad (2.15)$$

322 Given these definitions we can construct the QCD Lagrangian (\mathcal{L}_{QCD}) as shown in
323 eq. (2.16) where the gluon field tensor $G_k^{\mu\nu}$ is the one defined in eq. (2.17)

$$\mathcal{L}_{QCD} = \bar{q}(i\gamma_\mu D^\mu - m_q)q - \frac{1}{4} G_k^{\mu\nu} G_{k\mu\nu} \quad (2.16)$$

$$G_k^{\mu\nu} = \partial^\mu G_k^\nu - \partial^\nu G_k^\mu + g_s f_{klm} G^\mu G_m^\nu \quad (2.17)$$

324 The strong force is peculiar in that we experimentally observe only colorless objects in
325 the form of bound states of quarks known as hadrons. Qualitatively, when a bound
326 state of quarks (meson or baryon) is given sufficeint energy to separate the strong force
327 dramatically increases in strength. At the point where the objects would separate, and
328 thus no longer be colorless, it becomes energetically favorable to produce a quark/anti-
329 quark pair in a process known as hadronization. In other words, attempting to separate

330 a bound quark state into its colored constituents simply results in new colorless bound
 331 states. This requirement of colorless objects by the strong force is known as color
 332 confinement. For highly energetic strong interactions at hadron colliders the result is
 333 an expanding chain of hadronizing quarks and gluons and their decay products known
 334 as a jet.

335 2.4 The Higgs Mechanism

336 The Higgs Mechanism is the system by which the gauge bosons and fermions attain mass
 337 through the spontaneous breaking of the electroweak symmetry of the Higgs potential.
 338 This section will also discuss briefly the couplings of the Higgs boson to massive particles,
 339 as well as it's self couplings.

340 2.4.1 Electroweak Symmetry Breaking

341 The Higgs field is expressed as a complex doublet, Φ , and thus has four components as
 342 shown in eq. (2.18)

$$\Phi(x) = \begin{pmatrix} \phi^+ \\ \phi^0 \end{pmatrix} = \frac{1}{\sqrt{2}} \begin{pmatrix} \phi_1(x) + i\phi_2(x) \\ \phi_3(x) + i\phi_4(x) \end{pmatrix} \quad (2.18)$$

343 The four compoenents of this field each represent a degree of freedom which will be
 344 used to give the longitudinal polarizations of the gauge bosons W^\pm, Z and the mass of

the Higgs boson. The resulting lagrangian for the higgs includes a kinetic term (K) as well as the Higgs potential (V) all of which are invariant under the Electroweak gauge symmetry $SU(2)_L \times U(1)_Y$

$$\mathcal{L}_{\text{Higgs}} = \underbrace{(D_\mu \Phi)^\dagger D^\mu \Phi}_{\text{K}} - \underbrace{(\mu^2 \Phi^\dagger \Phi + \lambda (\Phi^\dagger \Phi)^2)}_{\text{V}} \quad (2.19)$$

Here we constrain $\mu^2 < 0$ and $\lambda > 0$ such that the potential forms a stable minima. The shape of this potential is shown in fig. 2.3 and is often referred to as the "Mexican-hat" or "Wine-bottle" potential.

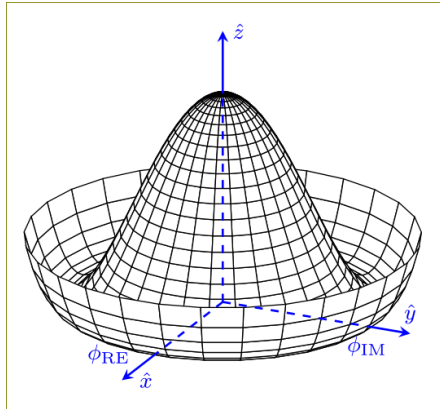


Figure 2.3: A lower dimensionality representation of the shape of the Higgs Potential. The central peak represents a $v = 0$ rotationally symmetric unstable state, while the trough represents the infinite choices of minima that can be selected upon the spontaneous breaking of symmetry.

Whatever you call it, this potential is significant in that its minimum is not at $\Phi = 0$ but instead is symmetric around the origin thus defining an infinite number of states

353 that minimize V . The value of this minima can be calculated by taking the derivative
 354 of V with respect to Φ and setting it equal to 0. This value, also known as the vacuum
 355 expectation value (vev) has been found to be $v \equiv \sqrt{-\mu^2/\lambda} = 246$ GeV. In order to reach
 356 this ground state energy, the Higgs field must spontaneously break this symmetry, and
 357 thus acquire an arbitrary single value. For ease of calculation we orient our coordinate
 358 system such that

$$\langle \Phi(x) \rangle = \frac{1}{\sqrt{2}} \begin{pmatrix} 0 \\ v \end{pmatrix} \quad (2.20)$$

359 Next we parameterize small perturbations around the minimum of the Higgs potential
 360 as

$$\langle \Phi(x) \rangle = \frac{1}{\sqrt{2}} \begin{pmatrix} 0 \\ v + h(x) \end{pmatrix} \exp \left(i \frac{\tau^i}{2} \theta^i(x) \right) \quad (2.21)$$

361 Here the real scalar field $h(x)$ corresponds to radial perturbations of the minima and
 362 while the three $\theta^i(x)$ are the Nambu-Goldstone fields with values determined by your
 363 choice of gauge. Choosing the unitary gauge of $\theta^i(x) = 0$ and expanding the kinetic

364 term of eq. (2.19) around the vev we get

$$\mathcal{L}_{\text{Higgs},K} = \frac{g^2 v^2}{8} \left((W_\mu^-)^\dagger W^{-\mu} + (W_\mu^+)^\dagger W^{+\mu} \right) + \frac{1}{2} \begin{pmatrix} W_\mu^{3\dagger} & B_\mu^\dagger \end{pmatrix} \mathbf{M}^2 \begin{pmatrix} W^{3\mu} \\ B^\mu \end{pmatrix} + \dots \quad (2.22)$$

365 Here the first term is the physical mass term for the W^\pm bosons where we have con-
 366 structed their charge eigenstates out of the $W^{1,2}$ fields like this $W^\pm = \frac{1}{\sqrt{2}}(W^1 \mp iW^2)$.
 367 The second term represents the mixture of the W^3 and B fields through the mass ma-
 368 trix \mathbf{M} . By diagonalizing this matrix and identifying the mass eigenstates we find the
 369 physical fields of the photon (γ) and the Z boson

$$\mathbf{M}_{\text{Diagonalized}}^2 = \begin{pmatrix} 0 & 0 \\ 0 & \frac{v^2}{4}(g_W^2 + g'^2) \end{pmatrix} \quad (2.23)$$

370 The upper left diagonal element corresponds to the massless photon while the lower
 371 right diagonal element gives the mass of the massive Z boson. This leaves us with the
 372 following masses for the 4 Electroweak bosons

$$m_W = \frac{1}{2} g_W v \quad , \quad m_Z = \frac{1}{2} v \sqrt{g_W^2 + g'^2} \quad , \quad m_\gamma = 0 \quad (2.24)$$

373 The masses of the W^\pm and Z gauge bosons can be related through the Weinberg angle

374 or mixing angle which

$$\theta_W = \cos^{-1} \left(\frac{g_W}{\sqrt{g_W^2 + g'^2}} \right) \rightarrow m_Z = \frac{m_W}{\cos \theta_W} \quad (2.25)$$

375 Using this definition we can write out the exact mixture of B and W^3 that make up the
376 photon and Z boson

$$\gamma = \cos(\theta_W)B + \sin(\theta_W)W^3 \quad (2.26)$$

$$Z = -\sin(\theta_W)B + \cos(\theta_W)W^3 \quad (2.27)$$

377 2.4.2 Fermion Mass Terms

378 In section 2.2 we saw that fermion mass terms violate gauge invariance due to the
379 mixing of the left and right chiral states. The Higgs mechanism again allows for a gauge
380 invariant method of generating mass terms but this time through the Yukawa coupling
381 of the Higgs field to the fermion fields. To see an example of this here is the Yukawa
382 coupling term for the electron doublet (Ψ_L) and singlet (Ψ_R) coupling to the Higgs field
383 (Φ) after spontaneous symmetry breaking giving it the form shown in eq. (2.21) where
384 we have again choosen the unitary gauge $\Phi^i(x) = 0$.

$$\mathcal{L}_{Yukawa} = -g_e \left[\bar{\Psi}_L \Phi \Psi_R + \bar{\Psi}_R \Phi^\dagger \Psi_L \right] \quad (2.28)$$

$$= -\frac{g_e}{\sqrt{2}} \left[\begin{pmatrix} \bar{\nu}_e & \bar{e} \end{pmatrix}_L \begin{pmatrix} 0 \\ \nu + h \end{pmatrix} e_R + \bar{e}_R \begin{pmatrix} 0 & (\nu + h) \end{pmatrix} \begin{pmatrix} \nu_e \\ e \end{pmatrix}_L \right] \quad (2.29)$$

$$= -\underbrace{\frac{g_e}{\sqrt{2}} \nu}_{m_e} (\bar{e}_L e_R + \bar{e}_R e_L) - \underbrace{\frac{g_e}{\sqrt{2}} h}_{g_{e,h}} (\bar{e}_L e_R + \bar{e}_R e_L) \quad (2.30)$$

385 And voila, we have successfully generated mass terms for our fermion field and main-
 386 tained the gauge invariance of our Lagrangian by using all gauge invariant fields. This
 387 operation has also left us with the second term which represents the coupling of the
 388 electron to the higgs itself thus giving us the form of it's coupling constant $g_{e,h}$. Using
 389 our newly found mass of the electron m_e we can write

$$g_{e,h} = \frac{g_e}{\sqrt{2}} = \frac{m_e}{\nu} \quad (2.31)$$

390 Thus we see that the coupling of the higgs boson to a fermion is indeed proportional to
 391 the mass of the fermion itself. In other words, the more massive a particle is, the more
 392 the higgs couples to it and vice versa.

393 2.4.3 The Higgs Boson

394 As we have seen this Higgs mechanism not only properly mixes the gauge fields thus
 395 providing them gauge invariant mass terms, it also properly combines the left and right

396 chiral states of fermions to produce their mass terms. The final step then is to determine
 397 an observable of the theory that can be tested in experiment, namely the existence of a
 398 massive scalar particle, the Higgs boson itself.

399 Turning our attention to the potential term (V) of eq. (2.19) and substituting in our
 400 definition for Φ given in eq. (2.21) we find

$$\mathcal{L}_{\text{Higgs,V}} = \frac{1}{2}\mu^2\nu^2 - \mu^2h^2 + \lambda\nu h^3 + \frac{1}{4}\lambda h^4 \quad (2.32)$$

401 Here the first term is constant and thus can be ignored. The second term is the mass
 402 term for the SM particle the Higgs boson, $m_h = \sqrt{-2\mu^2} = \sqrt{2\lambda}\nu$. Remembering that
 403 $h = h(x)$ was used for small radial perturbations of the Higgs field we can identify the
 404 Higgs boson simply as an excitation of the Higgs field. Finally, the third and fourth
 405 terms represent the Higgs boson self-couplings. With these couplings and mass terms
 406 in hand we can now move on to the experimental verification of this theory as discussed
 407 next in chapter 3.

408 Chapter 3

409 Boosted Higgs at the LHC

410 In chapter 2 I've shown how the higgs mechanism resolves inconsistencies of the model
411 surrounding the generation of gauge boson and fermion mass terms while also main-
412 taining gauge invariance. However to understand the search for and resulting discovery
413 of this SM Higgs boson requires the discussion of how one goes about producing and
414 detecting the physical object itself. In order to gather sufficient statistics to validate
415 the theory we require a collider capable of putting enough energy into a collision to
416 rapidly produce Higgs bosons for study. To this end the Large Hadron Collider (LHC)
417 discussed in chapter 4 was laboriously designed, funded, and constructed by the largest
418 international collaboration of scientists on the planet. In this chapter I will discuss the
419 relevant Higgs boson production mechanisms available at the LHC as well as the various
420 decay modes of the Higgs that were used for its discovery, and are currently used to
421 measure its properties.

3.1 Higgs Production Mechanisms

At the LHC the dominate production mechanisms for the higgs in order of decreasing cross section are: gluon-fluon fusion (ggF), vector boson fusion (VBF), vector boson associated production or “Higgsstrahlung” (VH), and associated production with $t\bar{t}$ ($t\bar{t}H$) and $b\bar{b}$ ($b\bar{b}H$). The cross sections with associated theoretical uncertainties for each is shown as a function of the center of mass energy \sqrt{s} in fig. 3.1 and the actual feynman diagrams can be seen in fig. 3.2.

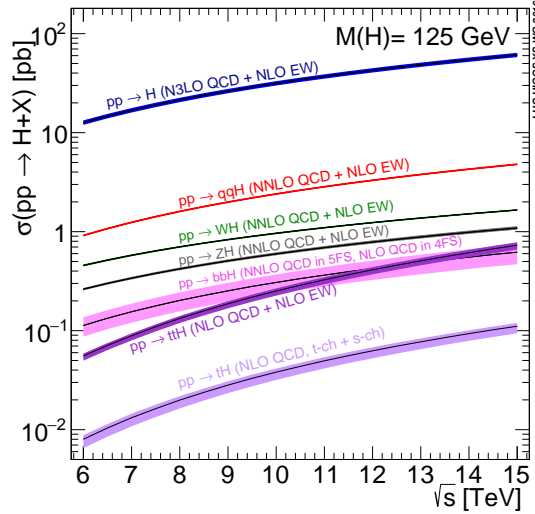


Figure 3.1: Cross section for the production of the SM Higgs boson as a function of the center of mass energy (\sqrt{s}) at the LHC. [1]

The dominant Higgs production mechanism at hadron colliders is ggF. This may seem strange as gluons are massless and thus do not couple directly to the Higgs. Instead the gluons indirectly couple to the Higgs via a quark loop. As discussed in section 2.4.2, the

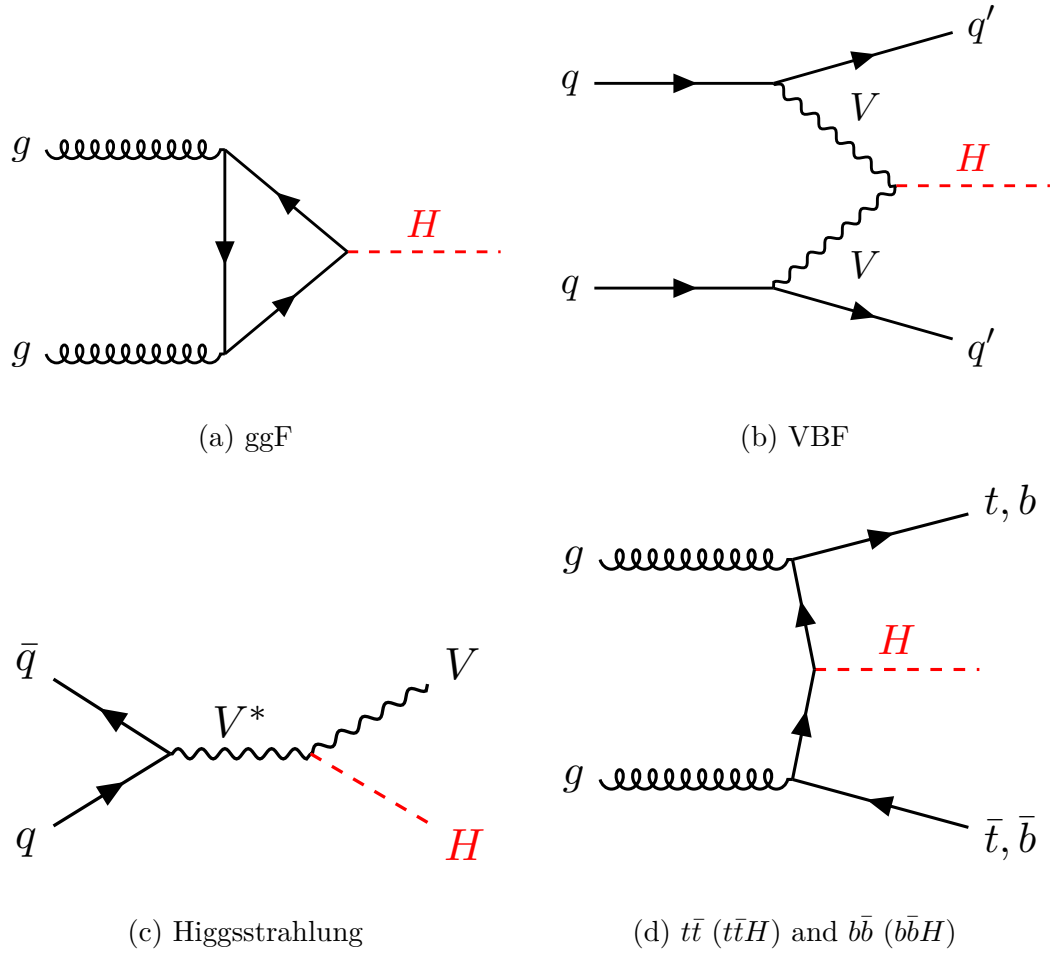


Figure 3.2: Feynman diagrams representing the dominant Higgs production modes at the LHC.

432 coupling of a fermion is proportional to m_f so the dominant contribution to this quark
433 loop comes from the top quark.

434 The second largest cross section for Higgs production at the LHC comes from the VBF
435 mechanism. In VBF the initial state quarks scatter via the exchange of a W^\pm or
436 Z boson which subsequently radiates the Higgs boson. Unlike ggF this production
437 mechanism scatters the initial state quarks which allows them to be observed as part of
438 the interaction. The existence of these extra quarks makes these interactions easier to
439 select for during analysis.

440 Next we have Higgs production in association with a vector boson. The cross section for
441 this is even lower than the above two, but remains important due to the easily selected
442 signature of the decaying vector boson. The largest background at the LHC is multijet
443 events coming from interactions that produce strong force objects. Thus the leptons
444 from the boson's decay act as a discriminator from this multijet background greatly
445 reducing its effect on sensitivity.

446 With the lowest cross section of the four methods discussed we have the production of
447 the Higgs in association with either $b\bar{b}$ or $t\bar{t}$. This channel is important due to our
448 ability to measure not only the Higgs, but also the quarks that it directly coupled with.
449 This allows us to directly measure the coupling of the Higgs to that quark, unlike the
450 ggF method where the quark in the loop is never directly observed.

451 As we can see, each of these methods has its advantages and disadvantages as well as

452 different valuable information that can be extracted. The result is a need for many
453 different analysis using different techniques to search for each mechanism.

454 **3.2 Parton Distribution Function**

455 The LHC collides protons, however looking at the feynman diagrams in fig. 3.2 we see
456 that it is quarks and gluons (a.k.a partons) that produce these fundamental interactions.
457 This is an indicator that when we calculate the production cross section for a process
458 at the LHC, we have to not only consider the hard-scatter probability of the specific
459 diagram, but also consider the composition of the proton itself. Specifically, we must
460 consider the fraction of the total momentum of the proton held by each of its constituent
461 partons. This concept is described by Parton Distribution Functions (PDFs) which give
462 the probability that the indicated parton carries momentum fraction x of the proton
463 when probed at with energy scale Q . An example PDF for $Q = 10\text{GeV}^2$ and $Q = 10^4\text{GeV}$
464 in fig. 3.3

465 **3.3 Branching Ratios**

466 The coupling of the SM Higgs with the gauge bosons and fermions has been shown to
467 give these particles their mass, however it also means that the Higgs can decay into all
468 of these particles.

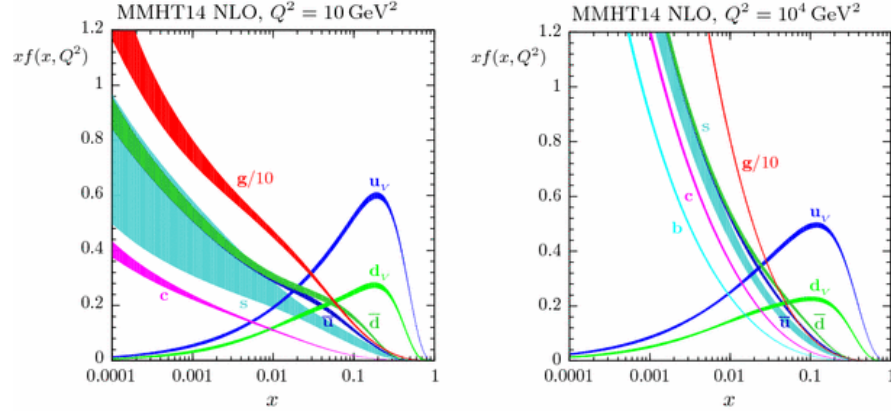
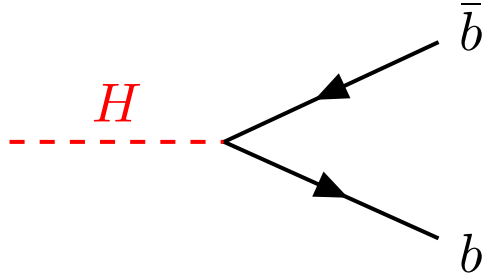
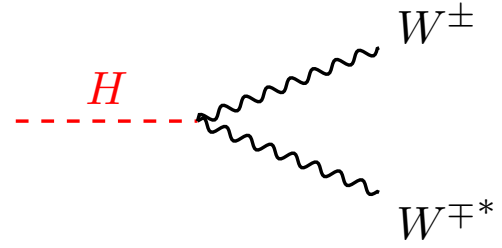


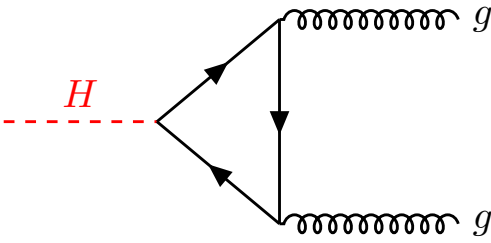
Figure 3.3: [2] MMHT2014 NNLO PDFs at $Q^2 = 10\text{GeV}^2$ and $Q^2 = 10^4\text{GeV}^2$ with associated 68% confidence-level uncertainty bands. The colored regions indicate the probability of finding the labeled parton with a momentum fraction given along the x axis. As expected the u_V and d_V contain the largest fraction of the momentum, however we can also see that many gluons will exist with smaller fractions of the total momentum. Note that as Q^2 increases you are more likely to find something besides a u/d



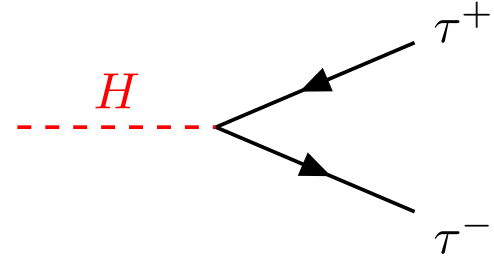
(a) $H \rightarrow b\bar{b}$



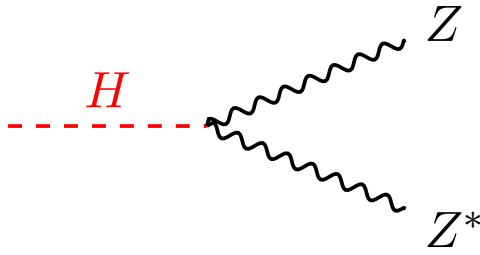
(b) $H \rightarrow W^+W^-$



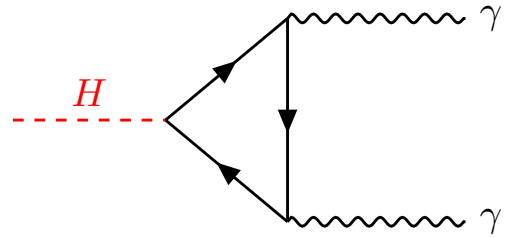
(c) $H \rightarrow gg$



(d) $H \rightarrow \tau^+\tau^-$



(e) $H \rightarrow ZZ^*$



(f) $H \rightarrow \gamma\gamma$

Figure 3.4: Feynman diagrams representing the leading Higgs decay channels.

Table 3.1: The branching ratios and the relative uncertainty for a Standard Model Higgs boson with $m_H = 125$ GeV [1].

Decay Channel	Branching Ratio	Relative Uncertainty
$H \rightarrow b\bar{b}$	5.84×10^{-1}	+3.2% -3.3%
$H \rightarrow W^+W^-$	2.14×10^{-1}	+4.3% -4.2%
$H \rightarrow \tau^+\tau^-$	6.27×10^{-2}	+5.7% -5.7%
$H \rightarrow ZZ$	2.62×10^{-2}	+4.3% -4.1%
$H \rightarrow \gamma\gamma$	2.27×10^{-3}	+5.0% -4.9%
$H \rightarrow Z\gamma$	1.53×10^{-3}	+9.0% -8.9%
$H \rightarrow \mu^+\mu^-$	2.18×10^{-4}	+6.0% -5.9%

469 3.4 Discovery

470 3.5 Boosted Higgs

471

Part II

472

Experimental Apparatus and

473

Associated Facilities

474 Chapter 4

475 The Large Hadron Collider

476 Located 100 meters under the Swiss / French boarder lies the 26.7 kilometer Large
477 Hadron Collider (LHC) [3]. The culmination of a huge international collaboration,
478 this apparatus is used to produce proton and heavy ion collisions for observation by the
479 four major experiments at the LHC: ATLAS, CMS, LHCb, and ALICE. The system was
480 designed for a maximum center-of-mass energy of $\sqrt{s} = 14$ TeV and a peak instantaneous
481 luminosity of $L = 10^{34} \text{cm}^{-2} \text{s}^{-1}$.

482 The first LHC workshop was held in 1984 in Lausanne at the European Organization
483 for Nuclear Reserach (CERN) [4]. The nearly 30 year old case for a machine that
484 would push towards the discovery of the elusive Higgs Boson was presented using the
485 existing CERN accerlerator facilities and the Large Electron Positron (LEP) collider
486 tunnel. The proposal became reality on September 10, 2008 when the first proton beams
487 were circulated, only to have calamity strike 9 days later in the form of a catastrophic

488 electrical fault. The repairs and improvements lasted until November 2009 when the
489 LHC restarted. Since then this modern marvel has worked wonderfully and, as hoped,
490 lead to the discovery of the Higgs Boson by the CMS and ATLAS collaborations July
491 4, 2013.

492 The following chapter provides a brief introduction to the worlds most powerful accel-
493 erator starting with the little red bottle of hydrogen in building XXX, and ending with
494 the interaction point where protons collide at the highest energies ever produced.

495 4.1 Particle Injecton Chain

496 We begin with the most common element in the Universe, hydrogen, as our source of
497 protons. A bottle of hydrogen gas provides 100 microsecond pulses of raw H_2 which
498 is then injected into a Duoplasmatron. There, a strong electric field and free elctrons
499 from a cathode ionize the molecule into bare H^+ aka a proton! These protons are
500 then accelerated by a 90kV field, leaving the Duoplasmatron with 1.4% speed of light
501 ($\sim 4000\text{km/s}$) or, in relativistic units, about 83KeV. The bare protons are then fed
502 into the accelerating RadioFrequency (RF) cavities of Linear Accelerator 2 (LINAC2).
503 Inside, conductors charged by a powerful oscillating electromagnetic field accelerate the
504 protons resulting in a 50MeV energy. Along the way, small quadrupole magnets shape
505 the proton packet insuring they remain in a tight beam. This pattern of accleration
506 with RF cavities and shaping/turnig with magnets is then repeated with CERN's first

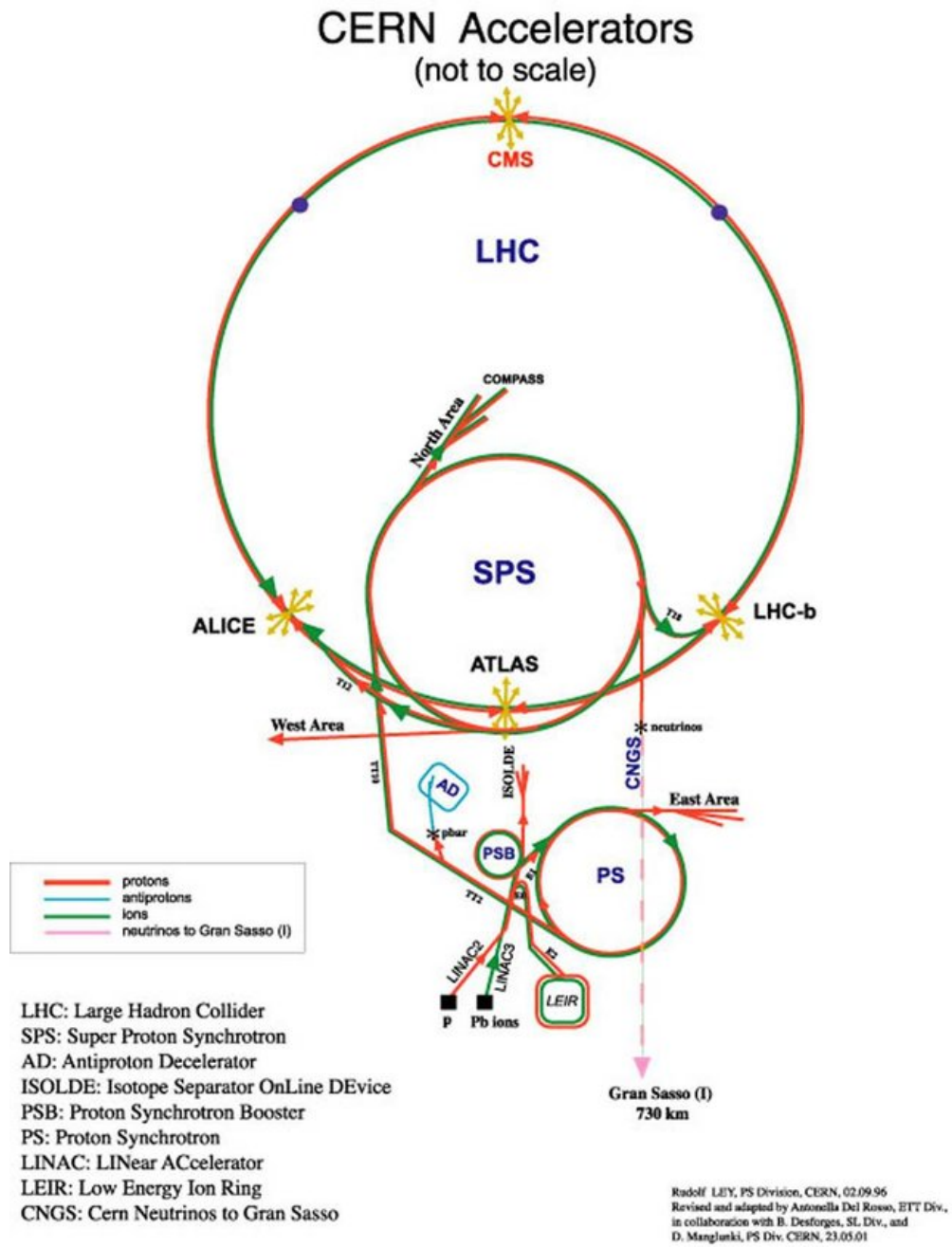


Figure 4.1: CERN accelerator complex

507 synchrotron, the Proton Synchrotron (PS) rendering a 1.4 GeV beam. The final step
508 before the LHC comes with the Super Proton Synchrotron where the same technologies
509 are implemented to produce 450 GeV protons, ready for injection into the LHC. A
510 diagrammatic representation of this chain can be seen in fig. 4.1

511 In order to produce proton-proton collisions the LHC uses two beams circulating in
512 opposite directions. The beams are not continuous, but instead consist of bunches, or
513 buckets, of $\mathcal{O}(10^{11})$ protons with a spacing of 25ns. Given the LHC circumference this
514 allows for 3564 buckets, however only 2808 are filled per beam due to safety requirements
515 and injection limitations. Each beam takes 4 minutes and 20 seconds to fill and then an
516 additional 20 minutes to for the protons to reach their maximum energy of 7 TeV TeV,
517 or 99.99999991% the speed of light! Under normal operating conditions these beams
518 can be used for many hours.

519 **4.2 LHC layout and design**

520 While often depicted as a perfect circle the LHC is in reality an octagon with rounded
521 edges, called arcs, as can be seen in fig. 4.2. Here you can see the counter circulating
522 beams of protons depicted in red and blue. These beams are focused and collided at
523 the 4 dedicated interaction points at rates of up to 40 MHz. Two of these points are
524 occupied by the ATLAS and CMS experiments, both of which are high luminosity,
525 multi-purposed experiments.

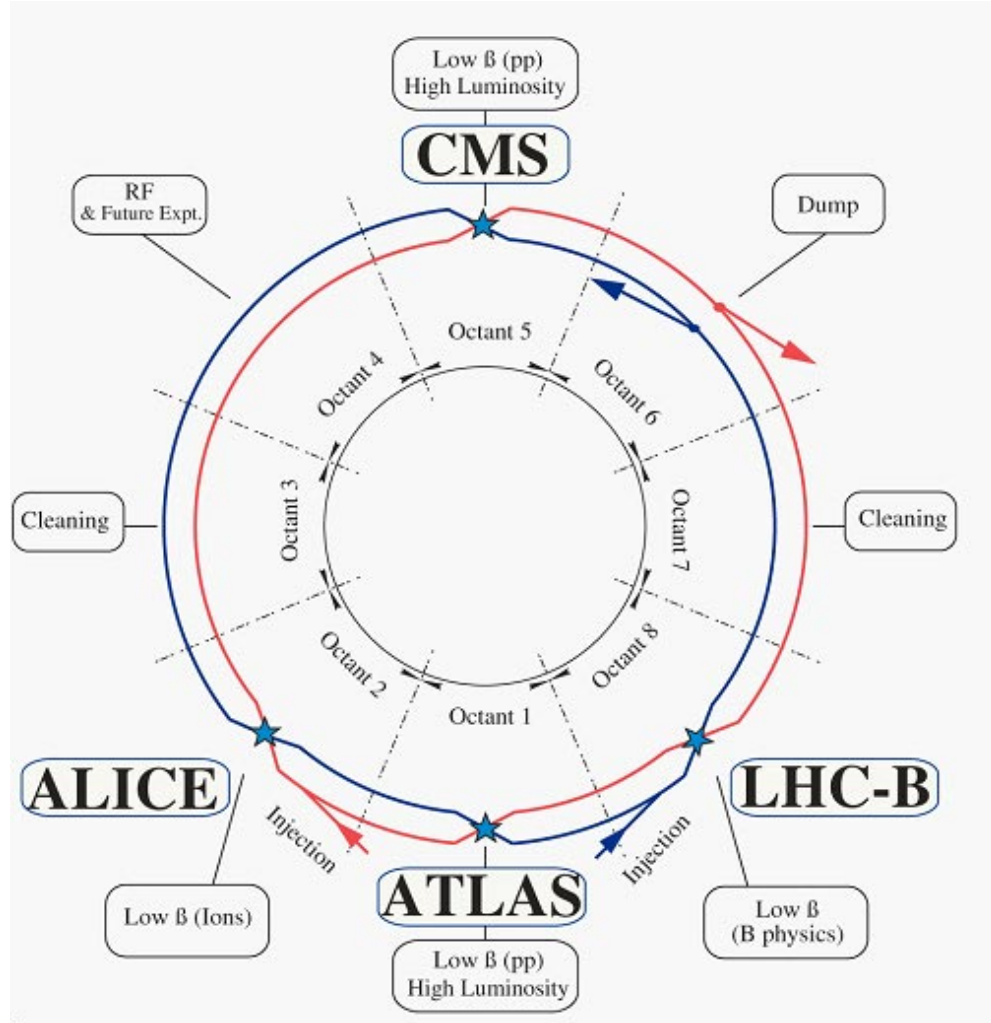


Figure 4.2: Labeled diagram of all the experiments at the LHC indicating the counter circulating beams and points of interest along the circumference of the accelerator.

526 The exact design of the tunnel is due to the experimental constraints of the original
 527 machine for which it was built, the Large Electron Positron (LEP) Collider. For the
 528 $\sim 2,000$ times lighter electron the maximum energy was limited by the synchrotron
 529 radiation, proportional to $\frac{1}{m^4}$, requiring long straight sections of accelerating RF cavities
 530 to recouperate the lost energy. Given that this effect is $\mathcal{O}(10^{13})$ times smaller for the
 531 proton the LHC is instead limited by our ability to design and construct magnets strong
 532 enough to bend the beam given the already determined curvature of the 8 arcs.

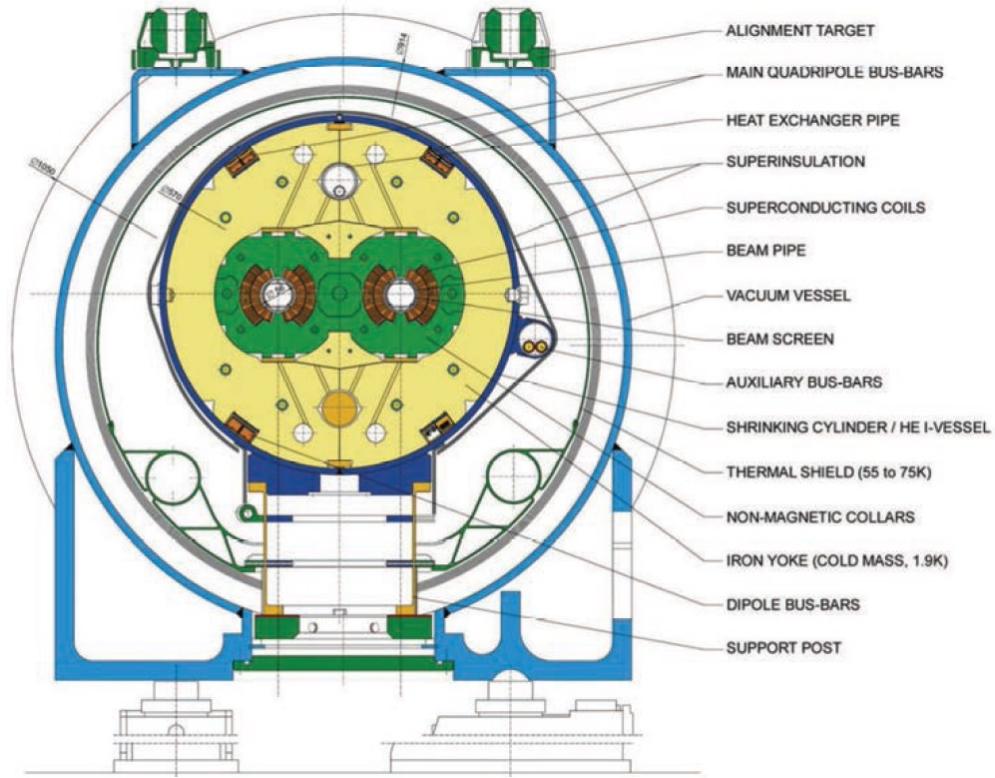


Figure 4.3: Depiction of a LHC dipole magnet 2-in-1 design labeling the major components

533 The oppositely circulating beams must each have their own ring and magnetic field
534 which lead to the creation of a twin-bore (i.e. "two-in-one") magnet design, a cross
535 section of which can be seen in fig. 4.3. These magnets are constructed using NbTi
536 superconductors which are cooled to 2K using superfluid helium. These magnets are
537 designed to provide the needed 8.33 T magnetic field required to bend the beams at the
538 design beam energy of 7 TeV. In total 1231 of these 15 m long bending dipole magnets
539 are used, in association with 392 5-7m long quadrupole magnets which are responsible
540 for keeping the proton bunches in a tight beam by squeezing them either horizontally
541 or vertically.

542 **4.3 Performance**

543 Since the begining of its stable running in 2010 the LHC has performed well, even
544 exceeding our expectations. While the experiment itself is incredibly complex, the
545 performance of the machine, for the purposes of our analysis, can be reduced to two
546 numbers; the familiar center of mass energy of the beams and a less common quantity
547 known as the integrated luminosity.

548 For particle physics the integrated luminosity is proportional to the total number of
549 collisions recorded during a specified time period, while the instantaneous luminosity is
550 proportional to the bunch crossing rate along with the cross section of a proton-proton
551 interaction and represents the potential number of collisions per second. Knowing this

we can see that the integrated luminosity, L_{int} is simply the integral of the instantaneous luminosity $L_{inst.}$ for a choosen data period as seen in eq. (4.1).

$$L_{int} = \int L_{inst.} dt \quad (4.1)$$

For a standard Gaussian beam, $L_{inst.}$ can be written as

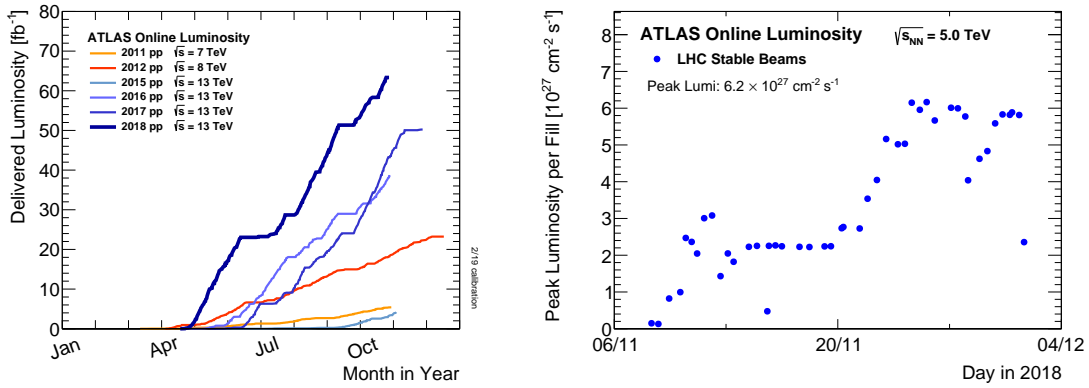
$$L = \frac{N_b^2 n_b f_{rev} \gamma_r}{4\pi \epsilon_n \beta^*} F \quad (4.2)$$

where N_b is the number of particles per bunch, n_b the number of bunches per beam, f_{rev} the revolution frequency, γ_r the relativistic gamma factor, ϵ_n the normalized transverse beam emittance, β^* the beta function at the collision point, and F the geometric luminosity reduction factor due to the crossing angle at the interaction point given by

$$F = \left(1 + \left(\frac{\theta_c \sigma_z}{2\sigma^*} \right)^2 \right)^{-1/2} \quad (4.3)$$

where θ_c is the full crossing angle at the interaction point, σ_z is the RMS bunch length, and σ^* is the transverse RMS beam size at the interaction point.

For the ATLAS experiment the integrated luminosity for each year can be seen in fig. 4.4a as well as an example of the instantaneous luminosity for the choosen year in fig. 4.4b.



(a) Integrated Luminosity 2011 - 2018 (b) 2018 Peak Instantaneous Luminosity

Figure 4.4: Luminosity is monitored as both a running total known as the Integrated Luminosity as depicted in (a) and as an instantaneous quantity as shown in (b)

4.4 Pile-up at the LHC

Given the large number of protons per bunch and the cross-section of a proton-proton interaction, the probability to observe multiple interactions per bunch crossing is quite high. These multiple-interaction are known as pile-up, μ or the time averaged representation $\langle\mu\rangle$, and come in two different forms:

1. **In-time pile-up:** These are the other proton-proton collisions that occur during the same bunch crossing as the primary interaction that caused the Data Acquisition (DAQ) system to trigger. These are the standard extra interactions we expect to observe as stated above.
2. **Out-of-time pile-up:** These are interactions that occur either before or after a

574 bunch crossing that causes the DAQ to trigger. This effect is generally due to the
 575 long integration times of some detector electronics.

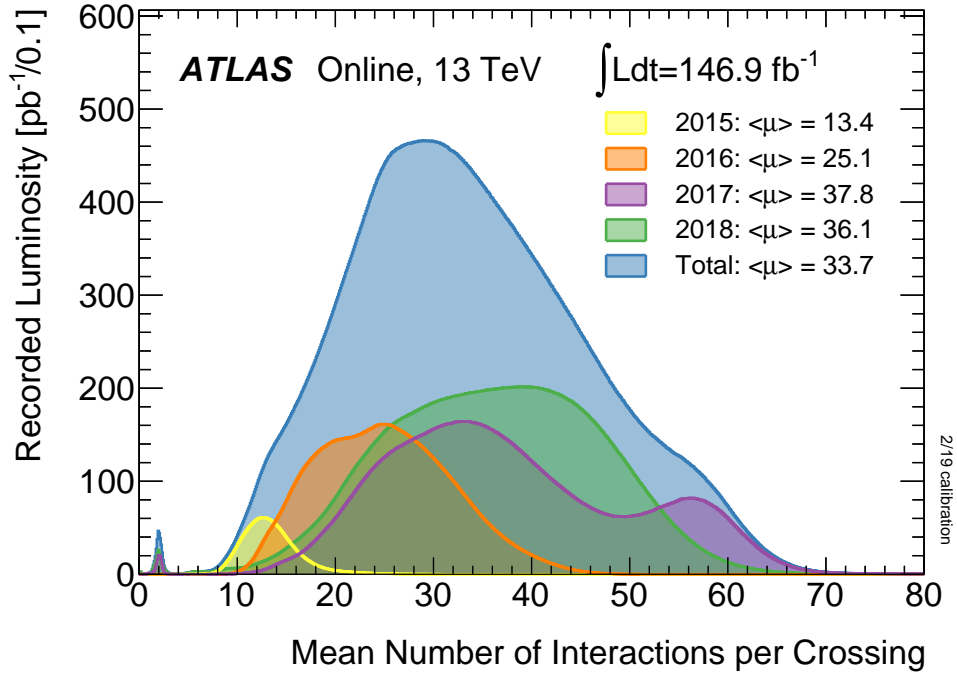


Figure 4.5: Pileup for data taking periods 2015 - 2018

576 The pile-up profile for past years can be seen in fig. 4.5. The width of this distributino
 577 is due a combination of Poissonian statistics, the decrease in number of protons per
 578 bunch over the lifetime of a single run, and optimization tweaks to the beam's profile
 579 during runtime. Understanding and eliminating the noise from these pile-up events is
 580 crucial to reconstructing physics variables to represent the primary interaction we hope
 581 to observe.

582 Chapter 5

583 The ATLAS Detector

584 Given the immense energies available at the LHC, and the veritable zoo of particles we
585 are trying to detect, we require a general-purpose experiment in order to fully exploit
586 the full range of physics opportunities provided. Two international collaborations rose
587 to this challenge, the CMS (Compact Muon Solenoid) and ATLAS (A Toroidal LHC
588 Apparatus) experiments. While both have similar physics goals and each of them
589 strengths and weaknesses, this dissertation will focus on the ATLAS experiment and
590 the intricacies of its three main sub-detectors and two massive magnet systems depicted
591 in fig. 5.1.

592 Originally proposed in 1994 the ATLAS experiment was completed in 2008. On July
593 4th, 2012 in a joint announcement the ATLAS and CMS experiments announced the
594 discovery of the long predicted Higgs Boson. The collaboration now boasts over 3000
595 physicists from 175 institutions spread across 38 countries and continues to probe

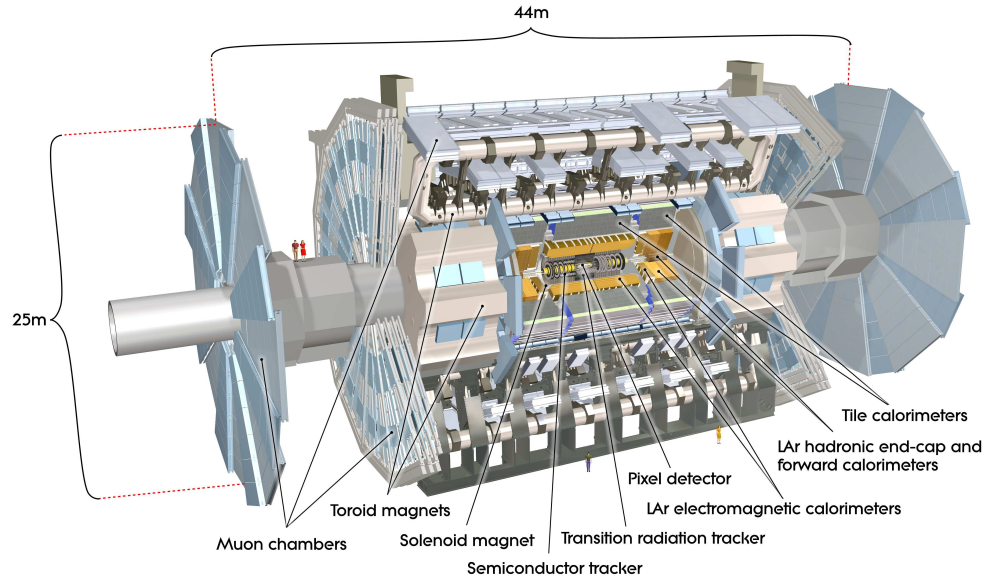


Figure 5.1: [5] Here we see a cut-away side view of the ATLAS detector with the major components labeled. Note that within each of these labeled components there may exist multiple different detector technologies. For scale two people in red are shown standing between the disk muon chambers on the left side of the figure.

596 the limits of the Standard Model in pursuit of answers to some of Humanities deepest
597 questions.

598 Located approximately 100 meters underground in a vast excavated chamber, the AT-
599 LAS detector rests its 7000 metric tonnes on a bed of concrete reinforced steel. Out of
600 it flows the signals of over 100 million electronic channels through a zip tied mass of
601 greater than 3000 kilometers of cabling. At its very center is one of the four interaction
602 points of the LHC, specifically Point 1, where the two counter circulating proton beams
603 are skillfully shaped and then collided by a series of magnets. The energetic particles
604 resultant from this collision then fly out in all directions into the bulk of the ATLAS
605 detector.

606 The first sub-system they meet is the Inner Detector (ID) and its many layers of strip
607 and pixel silicon detectors along with a transition radiation gaseous wire detector, all
608 bathed in the 2T magnetic field of the surrounding superconducting solenoidal magnet.
609 This system exploits the ionization of charged particles to track their curved trajectory
610 through the magnetic field. This curvature gives us charge information, a momentum
611 measurement, and precision 3D vertices crucial to the identification of the secondary
612 vertices of a b-hadron decay.

613 Outside of the solenoid the particles are faced with first the Electromagnetic and then
614 the Hadronic sampling calorimeters. Here, layers of scintillator and high radiation length
615 materials are implemented to measure the energy of electrons, photons, and hadrons.
616 As the goal is to completely absorb the energy of all outgoing particles the calorimeter

617 has a nearly 4π solid angle coverage.

618 Finally we have the muon system surrounding the calorimeter and equipped with its
619 own torroidal magnet system. Here the charged muon bends in the magnetic field
620 while leaving a trail of ionization in the muon spectrometer before exiting the detector
621 completely. Neutrinos are the only other standard model particle that leave the detector,
622 however they do so without detection. A depiction of the various particle interactions
623 with the different detector sub-systems can be seen in fig. 5.2

624 In the following sections I will explain our choosen coordinate system and give a more
625 detailed reveiw of these 3 detector sub-systems.

626 5.1 ATLAS Coordinate System

627 Using the nominal interaction point as the origin, ATLAS uses a right handed coor-
628 dinate system where the positive x -axis points towards the center of the LHC ring,
629 the positive y -axis points upwards, and the positive z -axis is defined by the counter
630 clockwise circulating beam direction as viewed from above shown in fig. 5.3 [5].

631 Using these coordinates we can define the physical momentum of the objects measured
632 as $\vec{p} = (p_T, p_z)$ with p_T being the momentum of the object in the transverse plane and
633 p_z the momentum along the beam axis. Given the cylindrical symmetry of ATLAS it
634 is desireable to define the polar angle θ from the beam axis with the $r - \phi$ plane being
635 perpendicular to that axis. Since the particles we observe are relativistically boosted

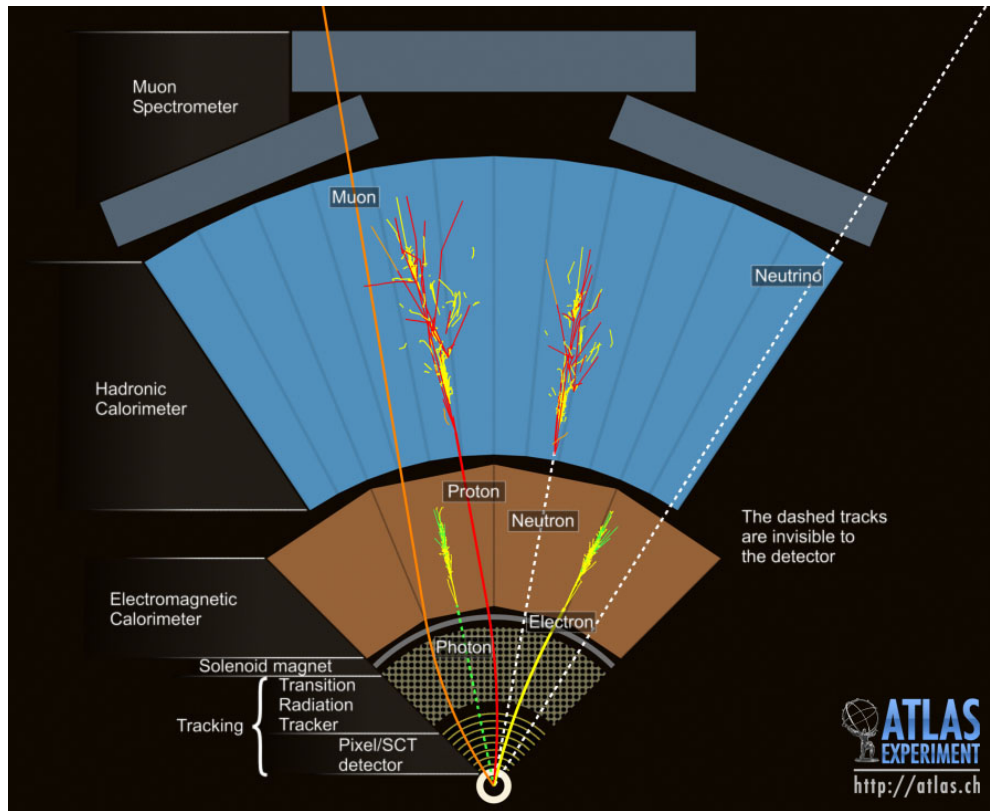


Figure 5.2: This slice of the ATLAS detector depicts how different particles interact with each component of the detector it crosses. A dashed line indicates no interaction while a solid line indicates interaction. Electrons (yellow/green) and charged hadrons (red) interact with the tracker and curve in the solenoid's magnetic field. Electrons and photons (yellow/green) are absorbed by the Electromagnetic calorimeter. All hadrons (red/yellow) are absorbed by the Hadronic calorimeter. The muons (orange) curve in both the solenoid and torroid magnetic fields before exiting the detector. Finally, the neutrinos (white) pass through the entire detector without interacting.

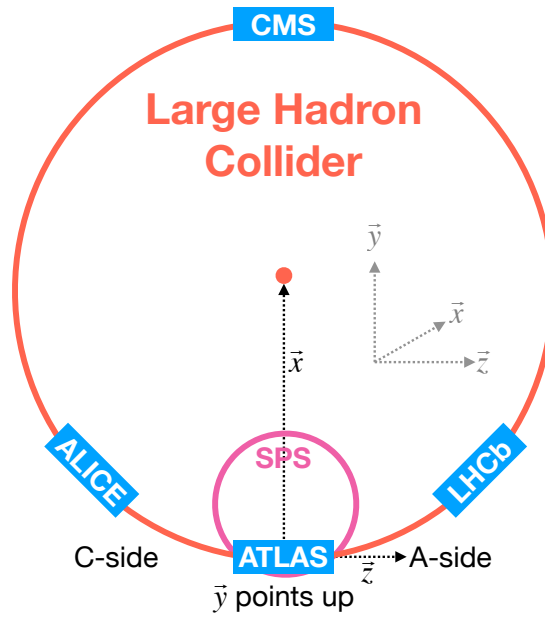


Figure 5.3: [6] A cartoon view of the the LHC from above showing the SPS, LHC and the four main experiments of the LHC: ATLAS, CMS, LHCb, and ALICE. The standard cartesian coordinate system is shown with its origin at the ATLAS interaction point, the positive x -axis towards the center of the LHC, the positive y -axis pointing upwards, and the positive z -axis pointing along the beamline towards the "A-side"

636 in the z -axis it is desirable to use the Lorentz invariant quantity pseudorapidity (η)
 637 defined in terms of the polar angle by

$$\eta = -\ln \tan \left(\frac{\theta}{2} \right). \quad (5.1)$$

638 where $\eta = 0$ is in the $x - y$ plane and larger values of $|\eta|$ being closer to the beam axis
 639 as can be seen in fig. 5.4.

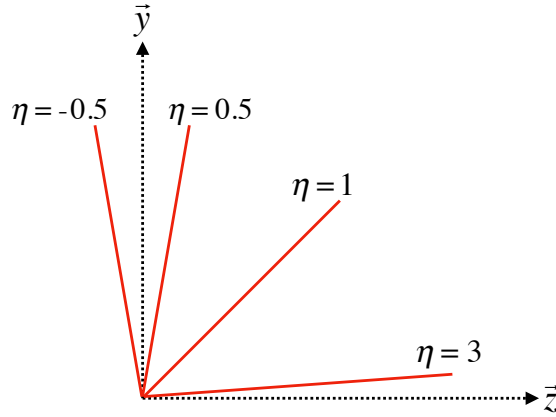


Figure 5.4: Modified from [6] this cartoon represents a selection of pseudorapidity (η) values overlaid with some cartesian coordinates (dashed black lines). The redlines are drawn for $\eta = \pm 0.5, 1.0, 3.0$

640 In this analysis the angular separation between objects in the detector is calculated and
 641 represented using the geometric quantity

$$\Delta R = \sqrt{(\Delta\eta)^2 + (\Delta\phi)^2} \quad (5.2)$$

5.2 Tracking with the Inner Detector

With its closest component, the insertable b-layer (IBL) [7], only 3.3 cm from the interaction point The Inner Detector (ID), shown in fig. 5.5 [8, 9], faces the incredible challenge of providing precision momentum resolution and identification of both primary and secondary vertex measurements of charged tracks all while receiving the highest fluence.

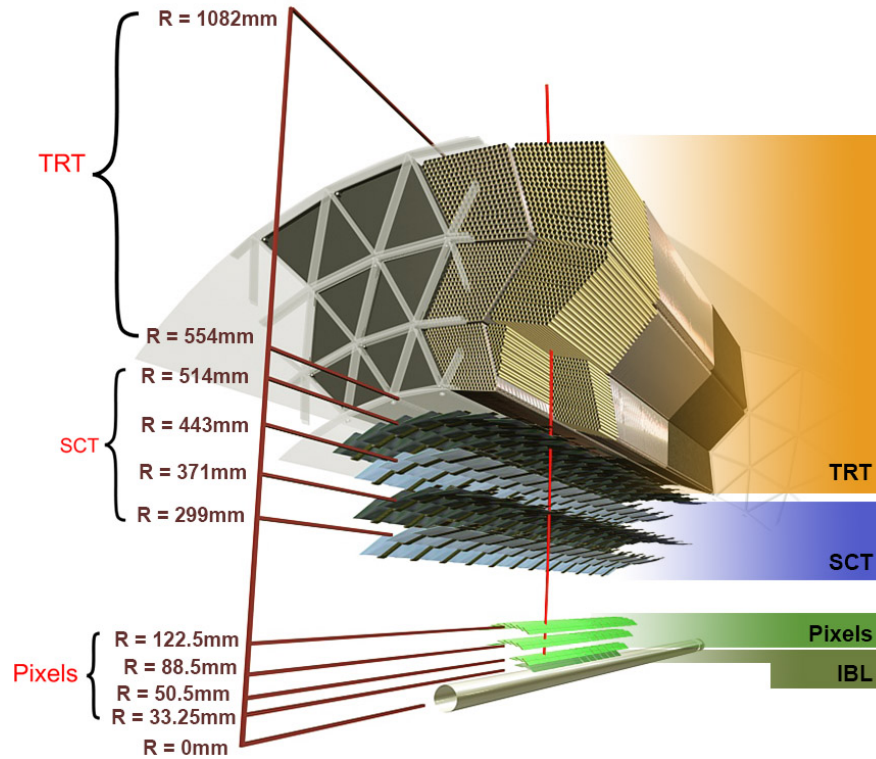


Figure 5.5: [7] Diagram of inner detector

It is designed to be very compact to reduce the probability of a particle decaying inside and to give precision measurements of the particles curvature in the 2T solenoidal

650 magnetic field. This leads to excellent momentum resolution above the nominal p_T
651 threshold of 0.5GeV and within the pseudorapidity range of $|\eta| < 2.5$ as shown in
652 fig. 5.6

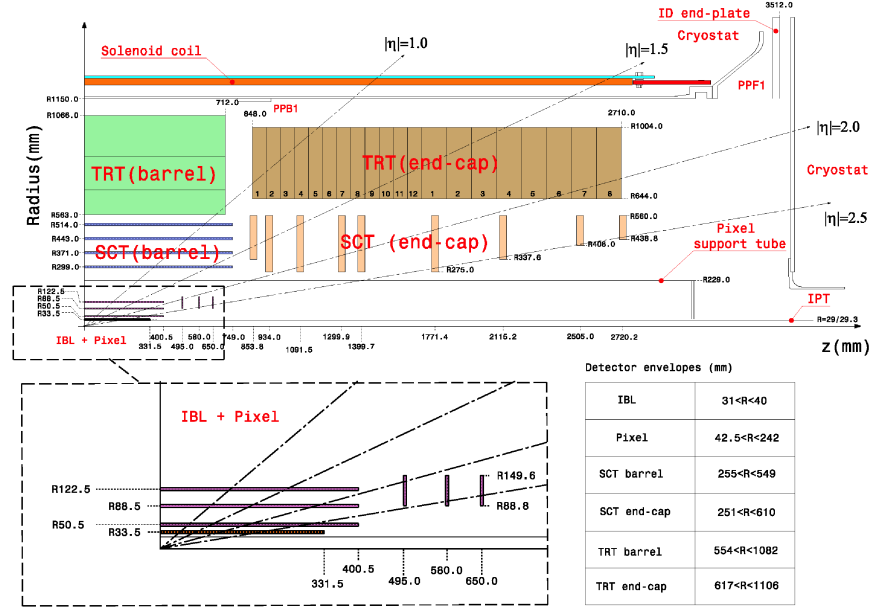


Figure 5.6: [10] Schematic of the Inner Detector including eta lines. Each component shown is cylindrically symmetric leading to a multi-layered detector.

653 The ID is composed of three different detector technologies for particle trajectory re-
654 construction: The Pixel Detector, Semiconductor Tracker (SCT) and the Transition
655 Radiation Tracker (TRT). These will be discussed in the following sections.

5.2.1 Pixel Detector

The ATLAS Pixel Detector [5], the innermost subdetector of the ID, is designed to give the best resolution possible as close as possible to the interaction point. This is accomplished using the 4 barrel layers and the 3 disks per endcap as indicated in fig. 5.6. The inner most barrel layer, the IBL, has pixel dimensions of $50\mu\text{m}(\hat{\phi}) \times 250\mu\text{m}(\hat{z}) \times 200\mu\text{m}(\hat{r})$. For the other layers the dimensions are $50\mu\text{m}(\hat{\phi}) \times 400\mu\text{m}(\hat{z})$ for about 90% of the pixels and $50\mu\text{m}(\hat{\phi}) \times 600\mu\text{m}(\hat{z})$ for the others, all with a thickness of $250\mu\text{m}(\hat{r})$. This gives a total active area of 1.88m^2 collected through 92.4 million readout channels, more than half of the total number of channels for ATLAS. This detailed charged particle information very close to the interaction point is crucial not only for pattern recognition for track reconstruction, but also for the reconstruction of the primary and secondary vertices intrinsic to the decay of a b -hadrons, a critical element of the analysis presented in this thesis.

5.2.2 Semiconductor Tracker

Encompassing the Pixel Detector, the Semiconductor Tracker (SCT) [5] is composed of double sided silicon microstrips modules. Each side of the 4088 modules is constructed out of two silicon strip sensors that are daisy chained together. The result is 768 composite strips each 12.6cm with an inter-strip pitch of $80\mu\text{m}$. In the barrel the strips are aligned with the \hat{z} direction, while in the end caps they are aligned with the \hat{r} direction. In both cases the separation of the strips is constant in $\hat{\phi}$. The two sides are

676 rotated with respect to each other by $40\mu\text{m}$ to allow for position measurement along the
 677 length of the strip. These modules are then used to tile the 4 barrel layers and 9 disks
 678 per endcap (18 disks in total) as seen in fig. 5.6. This design is chosen to ensure that
 679 each charged track interacts with 8 strip layers (equivalent to four space points). This
 680 information is used to further measure the momentum and impact parameter, and as
 681 well as vertex identification of charged particles.

682 **5.2.3 Transition Radiation Tracker**

683 The Transition Radiation Tracker [5], the outermost subdetector of the ID, provides
 684 tracking through the detection of transition radiation from ultra-relativistic charged
 685 particles for $\eta < 2.0$ using 350,000 drift tube channels also known as straws. The 4mm
 686 diameter straws are filled with a 70% Xe, 27% CO₂, and 3% O₂ gas mixture and a $31\mu\text{m}$
 687 diameter gold-plated tungsten wire anode at the center for the collection of the ionization
 688 signal. In the barrel 73 azimuthally symmetric layers of 144cm straws are oriented parallel
 689 to the beam pipe with an electrical division in the center of each allowing the two sides
 690 to be read out separately. For each endcap the straws are radially oriented in 160
 691 symmetric planes each containing 768 37cm long drift tubes shown in fig. 5.6. In both
 692 the barrel and the end caps polypropylene fibers (barrel) or foils (encaps) function as the
 693 transition radiation material which causes the relativistic charged particles to radiate
 694 and thus ionize the gas in the straw. The amount of transition radiation produced
 695 is proportional to the Lorentz factor meaning that lighter particles (e.g. electrons) will

696 produce more radiation. Thus, by defining a high and low threshold, we can identify
 697 tracks belonging to electrons by requiring they register more high-threshold hits. There
 698 are typically 36 TRT hits per charged track.

699 5.3 Calorimetry

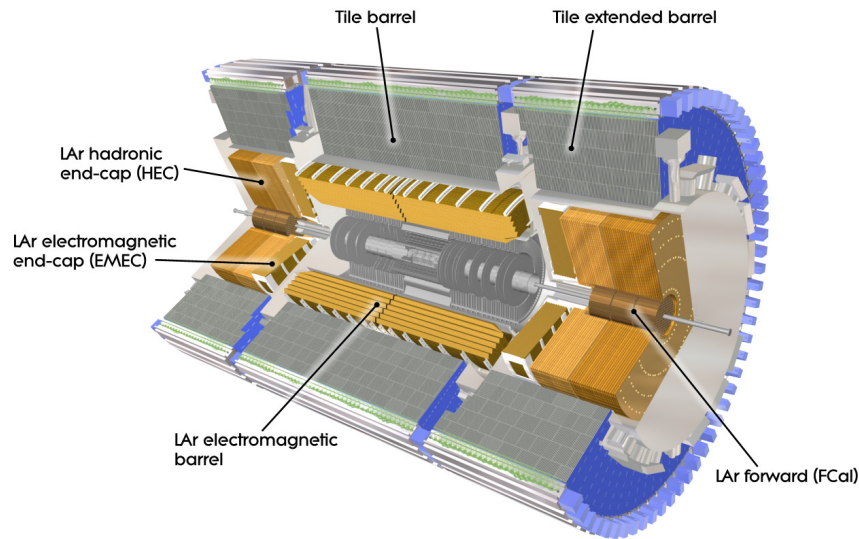


Figure 5.7: [5] A cutaway diagram of ATLAS's sampling calorimeters

700 Once the proton collision remnants have passed through the ID and it's surrounding
 701 solenoid they enter into the ATLAS calorimeters depicted in fig. 5.7. Sampling calorime-
 702 ter technologies were choosen for their compact geometry and lower cost point. These
 703 are constructed by alternating layers of absorber, a dense material which reduces the
 704 incedent particles energy, and active material which produces a detectible signal when
 705 a partilce passes through. This means that the detected signal is only a fraction of the

total energy of the particle and thus requires a study of the calorimeter response for calibration purposes [11]. The first system, the Electromagnetic Calorimeter (EMC), is designed to measure the energy of electrons and photons which primarily lose their energy via bremsstrahlung and pair production electromagnetic interactions. Outside of the EMC is the Hadronic Calorimeter (HC) which is designed to measure the energy of jets of hadrons through their electromagnetic and strong interactions. These detectors cover the entire $|\eta| < 4.9$ range and provide complete containment of both Electromagnetic and Hadronic showers with higher granularity in the EMC for $|\eta| < 2.5$, the region matched to the ID, for precision measurements of electrons and photons. By instrumenting this huge space in $|\eta|$ we can search for events with asymmetric energy deposits which imply the existence of a particle we didn't detect represented by missing transverse energy E_T^{miss} .

5.3.1 Electromagnetic Calorimeter

The innermost calorimeter, the Liquid Argon (LAr) Electromagnetic Calorimeter (EMC) [5], uses lead as the absorber and liquid argon as the active material in an "accordion geometry" as seen in fig. 5.8. This geometry was chosen for uniform coverage in $\hat{\phi}$ due to its lack of un-instrumented cracks in the radial direction. The barrel region covers $|\eta| < 1.475$ and an end cap on each side covers $1.375 < |\eta| < 3.2$ each housed in their own cryostat. The barrel is composed of two half barrels with a 4mm gap at $z = 0$ and both end caps are divided into an inner wheel covering $2.5 < |\eta| < 3.2$ and an outer

726 wheel covering $1.375 < |\eta| < 2.5$.

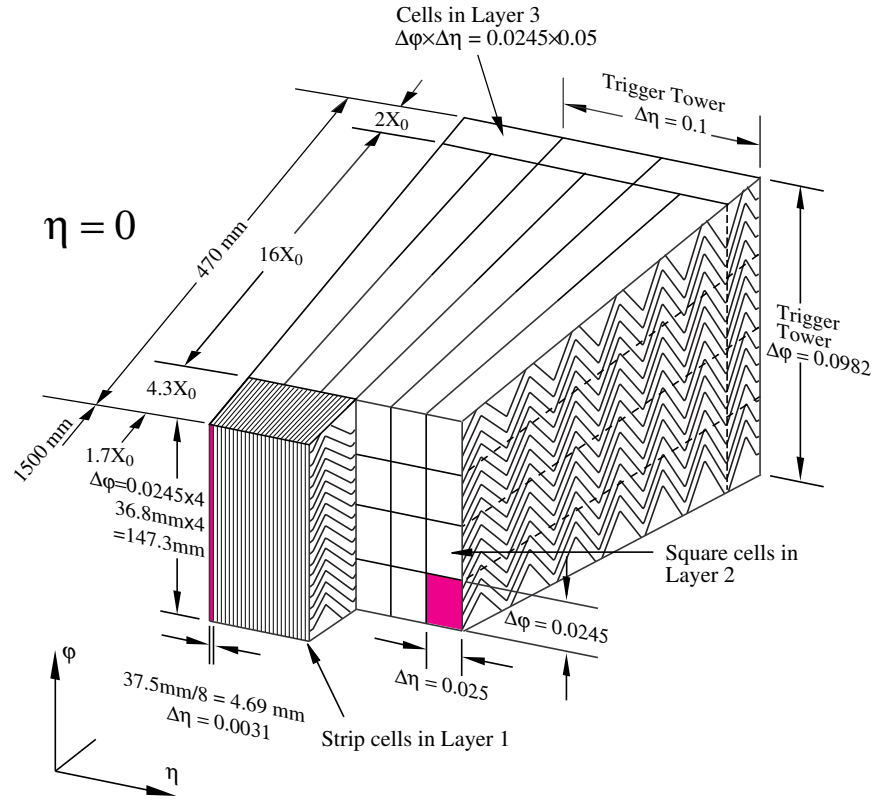


Figure 5.8: [5] Sketch of LAr EMC barrel module where the lead and liquid argon layers are visible in an accordion like geometry. Looking from the foreground to the back there are 3 different types of cells visible.

727 In the $|\eta| < 2.5$ region the EMC has 3 radial layers for precision physics measure-
 728 ments. Layer 1 consists of strip cells which are finely segmented with $\Delta\eta = 0.0031$
 729 and $\Delta\phi = 0.0245$ allowing for precision position resolution which gives discrimination
 730 power between a single γ deposit and the π^0 characteristic $\gamma\gamma$ deposit. Layer 2 , which
 731 collects the largest fraction of energy from electromagnetic shower, is segmented with

732 $\Delta\eta = .025$ and $\Delta\phi = 0.0245$. Layer 3 collects the tail of the electromagnetic shower
 733 using a coarser segmentation of $\Delta\eta = .05$ and $\Delta\phi = 0.0245$. Additionally, in the region
 734 $|\eta| < 1.8$ a thin pre-sampler , which contains no lead absorber, was placed in front of
 735 Layer 1 to allow for energy corrections due to losses upstream of the EMC. Combined
 736 the EMC is > 22 radiation lengths (X_0) in the barrel and $> 24 X_0$ in the end-caps,
 737 where a radiation length is the average distance an electron travels in a given material
 738 before losing $1/e$ of its original energy E_0 via bremsstrahlung radiation.

739 **5.3.2 Hadronic Calorimeter**

740 Directly outside the EMC envelope is the Hadronic Calorimeter (HC) system [5] which
 741 consists of three sampling calorimeter technologies: the Tile calorimeter, the LAr hadronic
 742 end-cap calorimeter (HEC) and the LAr forward calorimeter (FCal). Combined, these
 743 three subsystems give measurements of hadronic jet energies in the $0 < |\eta| < 4.9$ range.
 744 The tile calorimeter uses steel as the absorber layer and scintillating tiles as the active
 745 material and covers the region $|\eta| < 1.7$ with a barrel section flanked by two barrel ex-
 746 tensions each divided azimuthally into 64 modules. These scintillator tiles are read out
 747 on two sides by wave-length shifting fibers connected to photomultiplier tubes as seen
 748 in fig. 5.9. At $\eta = 0$ the total tile calorimeter thickness is 9.7 nuclear interaction lengths
 749 (λ), where λ is the average distance a hadron travels before interacting inelastically
 750 with a nucleus.

751 The HEC is composed of two independent wheels per end-cap located just past the

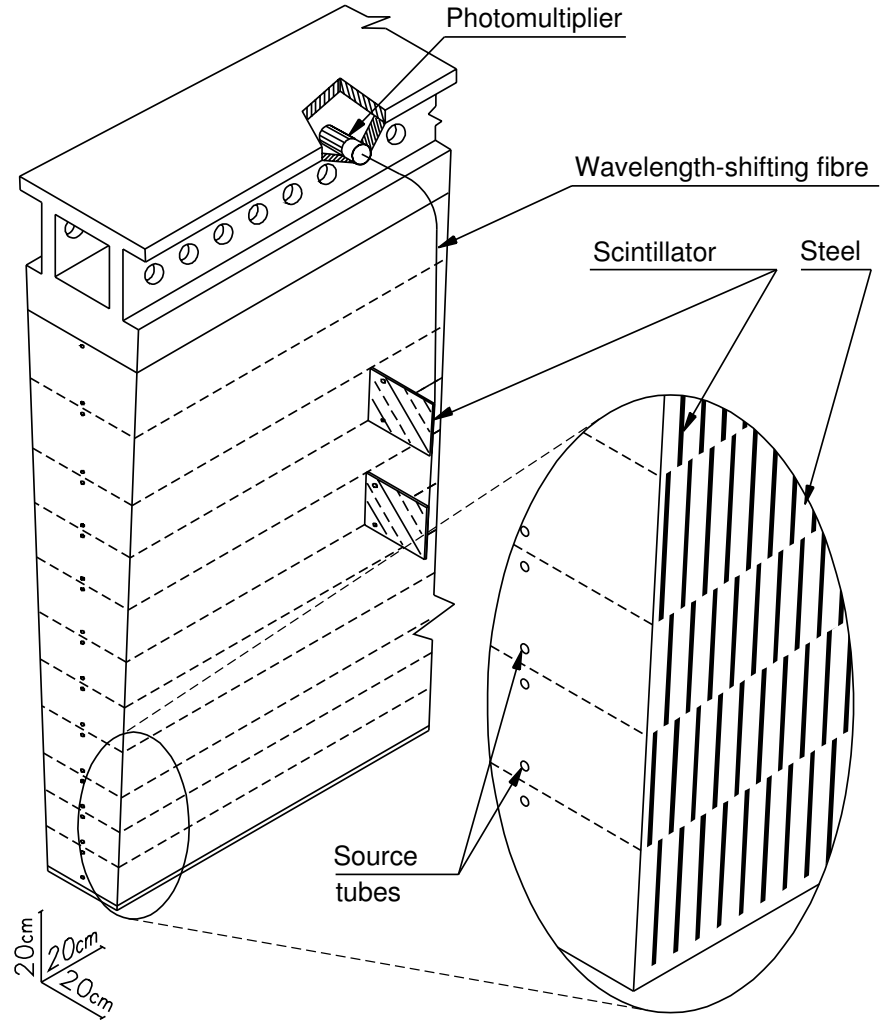


Figure 5.9: [5] Schematic of a tile calorimeter module including a depiction of the connection between the scintillator tile to the photomultiplier via a wavelength-shifting fibre.

752 EMC end-cap but sharing the same cryostat. This system uses copper as an absorber
753 and liquid argon for the active material and covers the $1.5 < |\eta| < 3.2$ range using
754 32 wdg-shaped modules per wheel. Finally, the FCal shares the same cryostat as the
755 EMC and HEC end-caps and acts to extend the coverage of the combined calorimeter
756 system to include the $3.1 < |\eta| < 4.9$ range. Each endcap contains 3 modules, the first
757 an electromagnetic module (Copper/Liquid-Argon) which is followed by two hadronic
758 modules which use (Tungsten/Liquid-Argon).

759 **5.4 Muon Spectrometer**

760 The ATLAS Muon Spectrometer (MS) [5], see fig. 5.10, accomplishes tracking of charged
761 particles in the $|\eta| < 2.7$ region for momentum reconstruction while also providing
762 triggering on charged particles in the $|\eta| < 2.4$ region. The magnetic field necessary for
763 momentum reconstruction is provided by 3 air core torroid systems, one barrel torroid
764 covering $|\eta| < 1.4$ and two endcap torroid systems which are inserted into the inner
765 radius of the the barrel torroid to cover the $1.6 < |\eta| < 2.7$. The so called transition
766 region $1.4 < |\eta| < 1.6$ between these two magnet systems is covered by a combination
767 of the barrel and endcap torroid magnets. Similar to the ID the resolution is inversely
768 proportional to the particle's incident momentum. Any muon with pT lower than 3GeV
769 will never make it to the MS and thus will not be detected.

770 Precision tracking measurements for momentum reconstruction is accomplished using

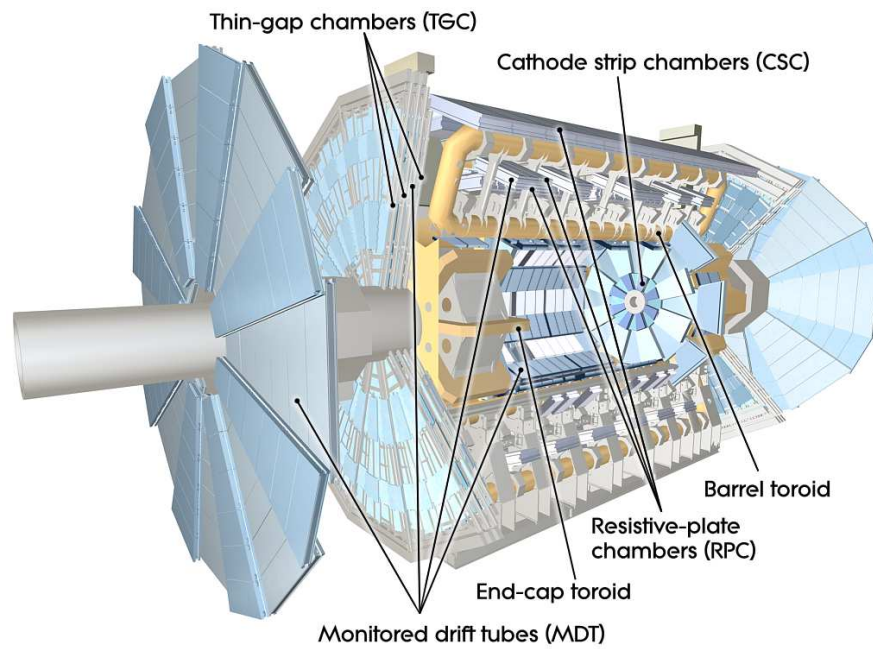


Figure 5.10: [5] A cut-away diagram of the ATLAS muon system and its many sub-detectors.

771 the Monitored Drift Tube chambers (MDTs) for $|\eta| < 2.0$ and using Cathode-Strip
772 Chambers (CSCs) for $2.0 < |\eta| < 2.7$. The MDT system consists of 1163 drift tube
773 chambers arranged in three to eight layers for varying η . The CSCs are designed to
774 withstand the higher rate and retain good time resolution using multiwire proportional
775 chambers with orthogonal segmented cathode planes.

776 The MS also gives nanosecond tracking information for triggering on muon tracks. This
777 is accomplished using Resistive Plate Chambers (RPC) in the barrel region $|\eta| < 1.05$
778 and Thin Gap Chambers (TGC) in the end-cap $1.05 < |\eta| < 2.4$ region. Both chamber
779 systems deliver a triggerable signal with a spread of 15–25 ns, thus providing the ability
780 to tag individual beam-crossings.

781

Part III

782

The HbbISR Analysis

783 Chapter 6

784 Data and Simulation Preparation

785 In order to compare data to theory ATLAS has developed an analysis chain which runs
786 both real data and simulated samples through the same processing, assuring a final
787 result which is as comparable as possible.

788 6.1 Data Used

789 6.2 Monte Carlo Samples

790 Chapter 7

791 Physics Object Selection

792 After the ATHENA Digitization step both data and monte carlo have the same format,
793 representing the three dimentional energy deposits. In order to analyze these deposits
794 they are cleaned, clustered and checked for overlap resulting in physics objects useful
795 for our specific analysis.

796 **7.1 Calorimeter Jets**

797 **7.2 Track Jets**

798 **7.3 Fat Jets**

799 **7.4 B-tagged Jets**

800 **7.5 Muons**

801 **7.6 Overlap Removal**

802 **Chapter 8**

803 **Event Selection**

804 Having created our physics objects we begin to make selections of what types of events
805 we want to consider given the goal of our analysis. In our boosted topology this means
806 considering things like momentum, jet collection efficiencies and background rejection.

807 **8.1 Selected Triggers**

808 **8.2 Pre-selection Studies**

809 **8.3 Signal Selection**

810 **8.4 Optimisation**

811 Chapter 9

812 Background Estimation

813 The dominant background was QCD. I worked on the $t\bar{t}$ control region. The V_{qq}
814 and single top backgrounds were estimated from monte carlo.

815 9.1 Multi-jet QCD estimation

816 9.2 $t\bar{t}$ control region

817 9.3 Single top estimation

818 9.4 Hadronic vector boson channel

819 **Chapter 10**

820 **Systematic Uncertainties**

821 **10.1 Theoretical Uncertainties**

822 **10.2 Experimental Uncertainties**

823 **Chapter 11**

824 **Statistical Fit**

825 The statistical fit in our analysis was accomplished using a framework developed for
826 Higgs searches.

827 **11.1 Profile Likelihood Function**

828 **11.2 Fit Configuration**

829 **11.3 Statistical Tests**

830 **Chapter 12**

831 **Results**

832 **12.1 Expectations**

833 **12.2 Statistical Analysis Results**

834 **12.3 Measurements and Limits**

835

Part IV

836

Conclusion

837 Chapter 13

838 Conclusion

839 I conclude that this section is the conclusion

Bibliography

- [1] Particle Data Group. “Review of Particle Physics, Chapter 11: Status of Higgs Boson Physics”. In: *Phys. Rev. D* 98 (3 2018), p. 030001. DOI: 10.1103/PhysRevD.98.030001. URL: <https://link.aps.org/doi/10.1103/PhysRevD.98.030001> (cit. on pp. 22, 28).
- [2] L. A. Harland-Lang et al. “Parton distributions in the LHC era: MMHT 2014 PDFs”. In: *The European Physical Journal C* 75.5 (May 2015), p. 204. ISSN: 1434-6052. DOI: 10.1140/epjc/s10052-015-3397-6. URL: <https://doi.org/10.1140/epjc/s10052-015-3397-6> (cit. on p. 26).
- [3] Lyndon Evans and Philip Bryant. “LHC Machine”. In: *JINST* 3 (2008), S08001. DOI: 10.1088/1748-0221/3/08/S08001 (cit. on p. 30).
- [4] Chris Llewellyn Smith. “Genesis of the Large Hadron Collider”. In: *Phil. Trans. Roy. Soc. Lond. A* 373.2032 (2014), p. 20140037. DOI: 10.1098/rsta.2014.0037 (cit. on p. 30).

- [5] ATLAS Collaboration. “The ATLAS Experiment at the CERN Large Hadron Collider”. In: *JINST* 3 (2008), S08003. DOI: 10.1088/1748-0221/3/08/S08003 (cit. on pp. 41, 43, 49–57).
- [6] Giordon Holtsberg Stark. “The search for supersymmetry in hadronic final states using boosted object reconstruction”. Presented 26 Apr 2018. May 2018. URL: <https://cds.cern.ch/record/2317296> (cit. on pp. 45, 46).
- [7] Karolos Potamianos. *The upgraded Pixel detector and the commissioning of the Inner Detector tracking of the ATLAS experiment for Run-2 at the Large Hadron Collider*. Tech. rep. ATL-PHYS-PROC-2016-104. 15 pages, EPS-HEP 2015 Proceedings. Geneva: CERN, Aug. 2016. URL: <https://cds.cern.ch/record/2209070> (cit. on p. 47).
- [8] *ATLAS inner detector: Technical Design Report, 1*. Technical Design Report ATLAS. Geneva: CERN, 1997. URL: <http://cds.cern.ch/record/331063> (cit. on p. 47).
- [9] S Haywood et al. *ATLAS inner detector: Technical Design Report, 2*. Technical Design Report ATLAS. Geneva: CERN, 1997. URL: <https://cds.cern.ch/record/331064> (cit. on p. 47).
- [10] B. Abbott et al. “Production and integration of the ATLAS Insertable B-Layer”. In: *JINST* 13 (2018), T05008. DOI: 10.1088/1748-0221/13/05/T05008. arXiv: 1803.00844 [physics.ins-det] (cit. on p. 48).

874 [11] Christian Wolfgang Fabjan and F Gianotti. “Calorimetry for Particle Physics”.
875 In: *Rev. Mod. Phys.* 75.CERN-EP-2003-075 (Oct. 2003), 1243–1286. 96 p. DOI:
876 10.1103/RevModPhys.75.1243. URL: <https://cds.cern.ch/record/692252>
877 (cit. on p. 52).

878 **Appendix A**

879 **Hadronic Vqq Sherpa Studies**

880 Ancillary material should be put in appendices, which appear after the bibliography.